

*Department of Construction Sciences*  
Solid Mechanics

ISRN LUTFD2/TFHF-2023/5256-SE(1-43)

# A comparison between tomographic and generated open cell metal foam structures

Master's Dissertation by  
Jonathan Ebbesson

Supervisor:  
Håkan Hallberg, Assoc. Prof., Division of Solid Mechanics

Examiner:  
Stephen Hall, Assoc. Prof., Division of Solid Mechanics

Copyright © 2023 by the Division of Solid Mechanics  
and Jonathan Ebbesson

Printed by Media-Tryck AB, Lund, Sweden

For information, address:

Division of Solid Mechanics, Lund University, Box 118, SE-221 00 Lund, Sweden

Webpage: [www.solid.lth.se](http://www.solid.lth.se)

## **Abstract**

This master thesis project presents steps on the image processing and reconstruction of an aluminium open-cell metal foam from  $\mu$ CT tomographic data. In addition, it also considers the generation of architecture foams using Voronoi Tessellation in combination with sphere packing algorithms. The process creates a foam skeleton which is used together with morphological operations such as dilation and hole closing with the purpose of obtaining a foam model. A parametric study is performed to observe the influence of the sphere packing input parameters on the architecture foam model. The final architecture models are similar both visually and geometrically to the reconstructed model. However, it is noted that a more complex image morphology might be required. The finite element meshing of both reconstructed and generated metal foams is also performed. By comparison it is shown how the temperature distribution differs between the foam models as opposed to a solid metal.

## Preface

This thesis project has been carried out at the Division of Solid Mechanics, Lund University, with the help of my supervisor Håkan Hallberg. I am very grateful for all the support and valuable input received from him during this work.

Even though the project ended up being quite different from what was initially planned and imagined, I found the time spent on it very enjoyable. It also allowed me to learn things within a field I was not previously familiar with.

# Contents

<b>1</b>	<b>Introduction</b>	<b>1</b>
<b>2</b>	<b>Metal foam classifications and properties</b>	<b>2</b>
2.1	Characterization . . . . .	2
2.2	Manufacturing . . . . .	3
2.3	Properties & Applications . . . . .	4
<b>3</b>	<b>Experimental characterization of metal foams</b>	<b>4</b>
3.1	Tomography . . . . .	4
<b>4</b>	<b>Image processing</b>	<b>6</b>
4.1	Image segmentation and binarization . . . . .	6
4.2	Extracting parameters from tomographic data . . . . .	7
4.2.1	Porosity . . . . .	7
4.2.2	Number of pores and cell radius . . . . .	8
<b>5</b>	<b>Virtual generation of foam models</b>	<b>9</b>
5.1	Classic foam models . . . . .	9
5.1.1	3D-construction based methods . . . . .	10
5.1.2	The Kelvin cell . . . . .	10
5.1.3	Voronoi tessellation and some generalizations . . . . .	11
5.2	Foam generation methods . . . . .	12
5.2.1	The (modified) force-biased sphere packing algorithm . . . . .	12
5.2.2	The Voronoi tessellation of a sphere packing . . . . .	14
5.2.3	Generating foam skeleton and image morphology . . . . .	14
<b>6</b>	<b>Mesh discretization</b>	<b>17</b>
6.1	Meshing parameters and extraction . . . . .	17
6.2	Delaunay triangulation . . . . .	17
<b>7</b>	<b>Flowcharts of algorithms</b>	<b>19</b>
<b>8</b>	<b>Results and discussion</b>	<b>21</b>
8.1	Reconstructed tomography data . . . . .	21
8.2	Architected foam samples . . . . .	24
8.2.1	Log-normal distribution . . . . .	24
8.2.2	Gaussian distribution . . . . .	28
8.2.3	Additional distributions . . . . .	30
8.3	Finite element mesh generation . . . . .	31
8.4	Thermal analysis . . . . .	34



# 1 Introduction

Metal foams have a wide range of applications and uses. They possess unique properties, being e.g. lightweight, highly energy-absorbing, and insulating materials, amongst other things [1]. However, they still remain fairly uncommon within the world of material science. This may be partly due to their fairly new introduction [2].

As such it would be of importance to study these materials in order to understand their properties and structural behaviour. This would both yield general information on foams and further extend their possible uses. Of interest is also the ability to create architected materials which mimic metal foam behaviour.

In recent years the properties, characteristics, and cellular structures of metal foams have been studied thoroughly. Extensive work has been performed on the 3D geometry reconstruction of metal foams images obtained from micro computerized tomography ( $\mu$ CT)-scans [3–8].

Using reconstructed tomographic geometries, Lautensack et al. [8] presented a method of estimating geometric characteristics based on image processing.

Another large area of investigation is in regards to the creation of generated foams. These are obtained using either a combination of generation algorithms or directly with data from  $\mu$ CT-scans [9–11]. Such constructed models aim to mimic the properties - both physical and geometrical - of real foams. They are sometimes referred to as architected foams.

These types of foam were investigated by Zhengwei et al. [9], who described the commonly used geometrical models used for architected foams. Of particular interest was the construction of foams based on Laguerre-Voronoi tessellations with respect to the method of randomly packed spheres. The structures of metal foams modelled by Laguerre-Voronoi tessellations was further investigated by both Wejrzanowski et al. [11] and Zhigang et al. [10].

Additional studies were provided by Bogunia et al. [5] who studied both tomographic reconstruction techniques and geometrically complex foams based on Laguerre-Voronoi tessellation. A different geometrical generation method based on the expansion of seeded ellipsoids with information from  $\mu$ CT images was proposed by Leblanc et al. [6].

For mechanical properties, Filice et al. [1] simulated the behaviour of aluminium in compression tests while Motz and Rippan [12] observed the deformation behavior of aluminium foams in tension. A summary of metal foam mechanical properties under tensile and shear stress was published by Kalpakoglou and Yiatros [13]. Additionally, mathematical relations for mechanical properties were derived by Gibson and Ashby [14] while Ashby [15] had previously presented general rules for cellular materials.

Regarding the thermal properties of metal foams, Singh and Kasana [16] presented information on the computational aspects of effective thermal conductivity of highly porous metal foams. Meanwhile, Ranut [17] discussed the existing empirical and analytical models for determining effective thermal conductivity of aluminium metal foams.

The combined image reconstruction and thermal response of metal foams has also been previously investigated. Amani et al. [3] studied the thermal conductivity both experimentally and by FE analysis using metal foam geometries obtained from X-ray tomography. In addition, Redenbech et al. [18] performed numerical calculations on the effective thermal conductivity of virtually generated foams obtained from Laguerre-Voronoi tessellations.

The particular combination of 3D image reconstruction, architected foam generation, and thermal analysis is the topic of this thesis project. More specifically, it aims to solve the following problems:

Firstly, the reconstruction of 3D-image data obtained from tomographic scans of an aluminium open-cell foam sample. Secondly, the creation of architected open-cell foam models based on foam generation algorithms. Such algorithms should preferably be able to use information from the reconstructed tomography data. Thirdly, using the reconstructed data and generated foam models to create appropriate FE meshes. Lastly, a finite element thermal analysis performed on both models as a means of comparison.

The image segmentation of tomographic data and virtual foam generation are to be performed in Matlab, specifically with the help of its image processing toolbox package. Subsequent thermal analysis simulations are performed in the finite element commercial software Abaqus.

## **2 Metal foam classifications and properties**

### **2.1 Characterization**

Metallic foams are characterized by a number of properties such a cell layout, morphology, porosity, and pore distribution [15].

Normally two initial distinctions are made between different types of metallic foams: open- and closed-cell foams. Both consist of pore and cell-like structures, with major differences being found in both appearance and physical properties.

The closed-cell types have pores surrounded by closed walls i.e. they are encapsulated by material. This compact arrangement often results in quite stiff structures [13].

In contrast, the open-cell foams contain interconnected pores and their

cell walls remain open to some extent. This instead produces rather soft, or elastic, structures [5].

Cell walls, i.e. the foam material, consist of a material network connecting all pores within the foam structure. Such material components are known as either struts or ligaments. The points where multiple ligaments are linked together are sometimes referred to as strut vertices. The position of both struts and pores are often considered non-deterministic due to the somewhat stochastic manufacturing processes and nature of metallic foams [4, 9].

A commonly used measure is the foam porosity,  $\theta$ , given by [5]:

$$\theta = \frac{V_p}{V_t} = \frac{V_p}{V_p + V_m}$$

where  $V_p$  is the total pore volume and  $V_t$  total volume of a given foam sample. The total volume can also be rewritten as the sum of the pore volume,  $V_p$ , and material volume,  $V_m$ . On the contrary, the material volume as a ratio of the total volume is given by the relative density,  $\rho_r$  [19]:

$$\rho_r = 1 - \frac{\rho^*}{\rho_s} = 1 - \theta$$

with  $\rho^*$  and  $\rho_s$  as the nominal and solid density, respectively.

As a rule of thumb, closed-cell foams normally have a low porosity,  $\theta < 0.3$ , while the opposite is true for open-cell foams,  $\theta > 0.7$ . In reality most metal foams consist of a combination of open- and closed-cell foams, often resulting in the need for more complicated classifications [5, 20].

## 2.2 Manufacturing

The basic manufacturing processes of metal foams were summarized by Ashby et. al [15], who originally presented the following possibilities: liquid metallurgy, coating techniques, and powder metallurgy. However, in recent years primary methods have shifted towards either liquid metallurgy or powder metallurgy, with liquid metallurgy being the more popular option. This is mostly due to the possibility of creating inexpensive materials with sufficient properties [21].

The liquid metallurgy process involves the adding of either foaming agents or gas particles into a furnace containing liquid metal. An example of a foaming agent is  $\text{TiH}_2$ . The combined melt is stirred to distribute both the agent and metallic particles evenly and thereafter removed from the furnace to allow for cooling. The resulting foam is a block containing pores positioned randomly within the metal. The pores are situated in way such that the



surface energy of the material is minimized [2]. The final pore sizes are proportional to the sizes of injected particles [22].

On the other hand, powder metallurgy is the process of mixing two powders: the desired metal and a foaming agent, normally  $\text{TiH}_2$ . After mixing, the combined powder is compressed into a solid shape which is heated within a furnace to allow for the foaming agent to expand. Alternatively, a solid space holder may be introduced instead of a foaming agent. In such a case, a similar process of compression occurs, followed by the removal of the shape holder during either heating or dissolution. Common space holders include salts, e.g.  $\text{NaCl}$  or  $\text{K}_2\text{CO}_3$ , or polymeric materials [20].

As for specific materials, aluminium is the most commonly used which is also attributed to its properties [2].

### 2.3 Properties & Applications

Due to their geometrical structure, metal foams possess interesting physical and mechanical properties. As an example, open cell foams, which are considered lightweight materials due to their high porosity, possess extremely high strength-to-weight ratio [4].

Expanding on the characteristics of other porous materials, Gibson and Ashby [14] linked the mechanical properties of metal foam to their structural properties such as porosity. These relations were based on both experimental and empirical data.

The open cell foams also have good thermal properties such as high thermal conductivity. On the other hand, closed cell foams have worse thermal capabilities but instead excel on the mechanical side of things, such as stiffness and strength. Additional properties of metallic foams include, but are not limited to, high energy-absorption, sound absorption, heat insulation and electrical applications [2, 20, 21].

In terms of specific applications, the list can be made long and includes, amongst others, the automotive and aerospace industry due to energy-absorption and lightweight properties [23]. Further applications include heat exchange devices such as heat ex-changer, radiators, etc. [20].

## 3 Experimental characterization of metal foams

### 3.1 Tomography

To properly understand and visualise material behaviour on a smaller scale micro X-ray computed tomography(CT) is often used. It is based on the

same working principles as as medical CT scanner but its design purpose differs. The main goal in regards to material sciences is instead the capture of high-resolution images of material data on a microstructural level[24]. A simple setup of such a system is depicted in Fig. 1.

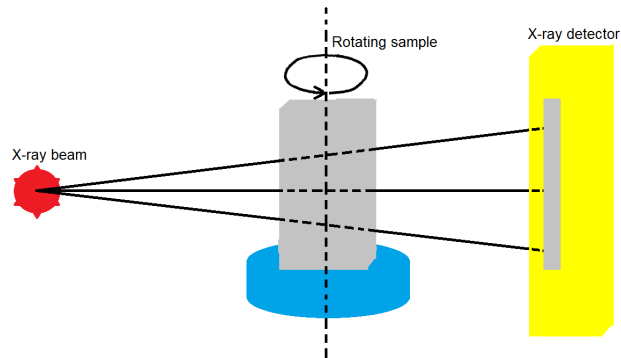


Figure 1: A simple schematic of the X-ray  $\mu$ CT process.

In short, the process begins by placing a material sample in the trajectory of a X-ray beam. By interacting with the material, some of the X-rays, or waves, are absorbed while others are transmitted. The transmitted waves are converted into visible light with the help of a scintillator. A camera detector is used to turn this light into a two dimensional contrast based intensity projection of the sample. By rotating the sample, a finite number of 2D projections are captured from different angles. A reconstruction algorithm uses a sum of all such two dimensional projections to create a 3D image of the sample [25].

Normally, the contrast in the 2D projection is due to different absorption coefficients at the material microstructural level. Alternatively, a phase contrast approach might be also considered if the absorption coefficients in the material are similar [26]. A possible scenario would be if the sample contains materials with equal atomic numbers since the absorption would be the same [24].

## 4 Image processing

### 4.1 Image segmentation and binarization

For 3D-image reconstruction, two dimensional image slices obtained from tomography are layered on top of each other. Each slice is mapped onto a grid-based image matrix of size equivalent to the provided image. Every position  $(i, j)$  on the 2D-grid represents a computerized pixel with a singular intensity value.

By stacking all slices, a 3D-image is assembled. This image consists of matrix position indices  $(i, j, k)$  with corresponding intensity values  $I_{ijk}$ . The position and its associated intensity value is normally referred to a voxel in 3D-space, as opposed to a pixel in two dimensions.

A two and three dimensional grid representation are shown in Fig 2a and Fig 2b, respectively. The intensity of each pixel or voxel is depicted as a random color for simplicity.

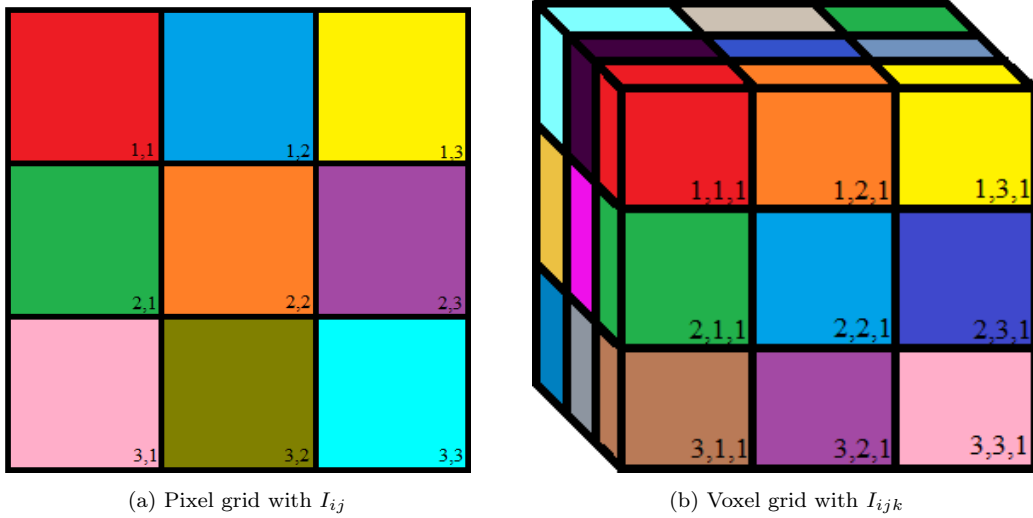


Figure 2: Grid-based structure with a random colour depicting the pixel and voxel intensities.

The resulting reconstructed 3D-image matrix becomes a grayscale image, i.e. an image containing varying intensities. To further process the image, binarization of the intensity data,  $I_{ijk}$ , is required. This can be described by the following threshold equation:

$$I_{ijk} = \begin{cases} 1, & \text{if } I_{ijk} > T \\ 0, & \text{otherwise} \end{cases}$$

where  $T$  is the global threshold, or cutoff value, of image  $I$ .

The value of  $T$  can be obtained using multiple algorithms, with the global Otsu threshold method being commonly chosen [5, 27]. This method extracts the cutoff value as a function of the maximum variance between intensity peaks of the image intensity histogram [28]. By employing the threshold, a fully binarized image is obtained, comprised solely of ones (material data points) and zeros (pores). A 2D slice of tomography data is shown in Fig. 3a and Fig 3b before and after binarization, respectively.

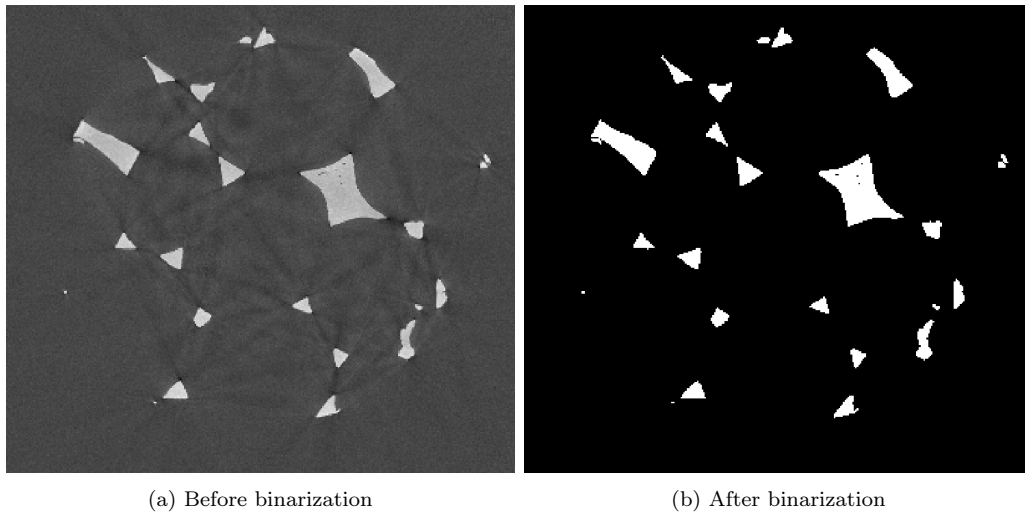


Figure 3: Binarization of tomography data slice.

## 4.2 Extracting parameters from tomographic data

### 4.2.1 Porosity

Expanding upon the porosity definition provided in Chapter 1, a slightly different numerical approach is used to find a measure of the porosity from tomography data. It can be summarized as the following:

Given a binarized 3D-image,  $I$ , calculate the relative density as the ratio between the number of material voxels and the total number of image voxels.

That is, find the ratio of data points equal to one as compared to the sum of all data points. A reverse calculation instead provides the porosity.

However, since the foam investigated is of cylindrical shape, the sum of data points is taken as a cylinder rather than the box in Fig. 3b. That is, image voxels outside this cylinder are not considered for the porosity calculations. An identical approach is taken when extracting the number of pores and pore radius.

#### 4.2.2 Number of pores and cell radius

By employing certain algorithms on the binarized image, it is also possible to obtain information regarding the number of pores and pore sizes of the foam. A frequently used method involves the use of level-set based image processing techniques [5, 6, 8].

In short, this can be performed by first finding the distance transform and its complement, of a provided binary image. The distance transform is an intensity image based on the Euclidean distance from a nonzero pixel or voxel. The further away from a nonzero value, the larger the value at a given position. Consequently, the complement instead provides information regarding the distance from pores to material, i.e. it finds distinguishable pore centers. Such a distance transform is depicted in Fig. 4a while its complement is shown in Fig 4b.

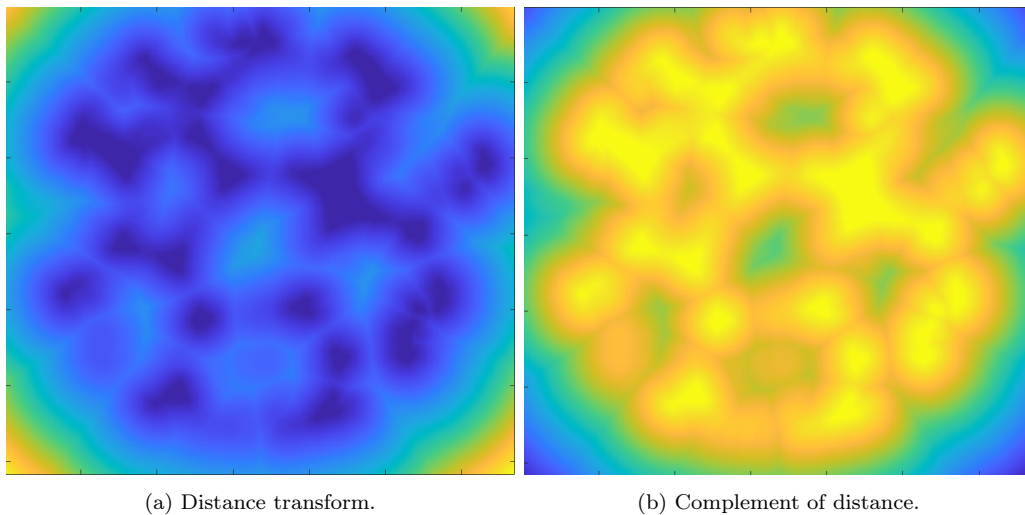


Figure 4: Distance and complement distance transforms of the binarized image.

Afterwards, a watershed transformation of the complement distance is performed. This creates isolated areas based on the pore centers obtained from the complement distance. Thus, each watershed region is the approximation of a pore within the sample. These can also be seen as the creation of basins with ridges along the perimeter of each region. The watershed transform is simply the filling of each separate water basin.

Lastly, a masking of this watershed results in a labeled version of the original binary image. Each labeled region represents a pore. To avoid over-segmentation, the suppression of localized peaks is performed prior to watershed transformation. The watershed and subsequent masking are shown in Fig. 5a and Fig. 5b respectively.

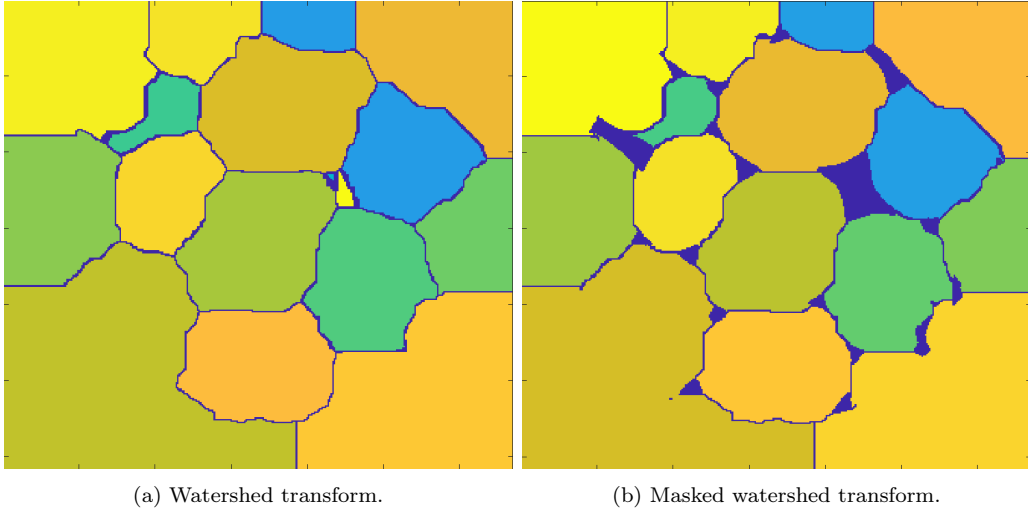


Figure 5: Watershed and subsequent masking.

By extending the distance-watershed transform to the three dimensional space, information regarding the number of pores and approximate pore sizes can be extracted. The number of pores is determined by the unique number of watershed regions. To extract a pore radius, each watershed region is first approximated as a sphere. Since each region is labeled, it is possible to find the volume of a sphere by counting the number of voxels with a specific label. Knowing the volume, it is thereafter trivial to calculate a sphere radius. The sum of all such sphere radii divided by the number of watershed region determines the average pore radius. These extracted values may later be used as input parameters in a virtual foam generation algorithms.

The implementation of such methods exist in the image processing toolbox of Matlab as the routines *bwdist* and *watershed*. The routine *imhmax* performs suppression of localized peaks.

## 5 Virtual generation of foam models

### 5.1 Classic foam models

As described by Zhengwei et al. [9], three common techniques exist for the virtual generation of metal foams: the direct 3D-reconstruction, Kelvin multi-cells, and Voronoi-based methods.

### 5.1.1 3D-construction based methods

The 3D-reconstructed technique is identical to the method of image based reconstruction described in Section 4.1. These models are matched with a scanned foam sample. Therefore, any results obtained from the subsequent reconstruction-based simulations would be unique and only valid for the specific sample. The process of obtaining and reconstructing such samples may also be computationally expensive [9].

### 5.1.2 The Kelvin cell

The Kelvin multi-cell method is the stacking of unit cells with some deterministic shape. The shape itself was originally described by Lord Kelvin and was based on the shape of the bubble packing patterns in foam structures [29]. Its geometrical shape, also referred to as a tetrakaidecahedron, is depicted in Fig 6a while the stacking of such cells is shown in Fig. 6b.

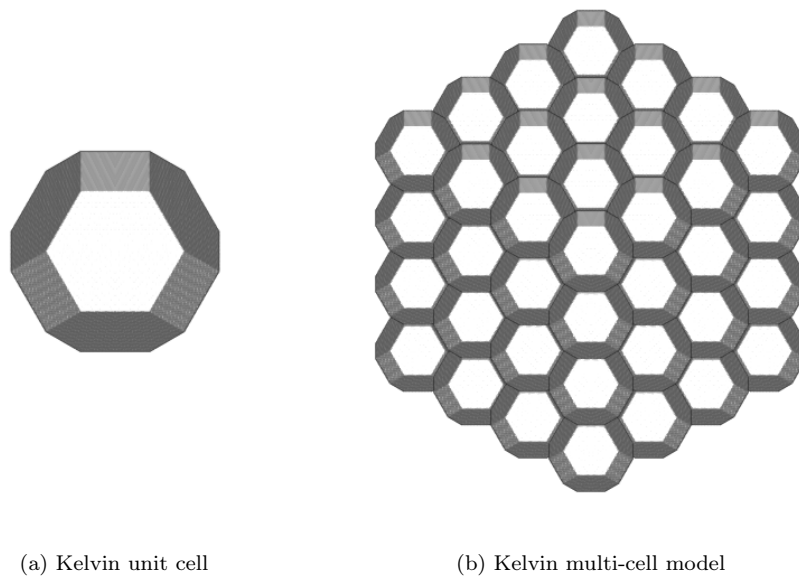


Figure 6: Kelvin cell and the corresponding stacking of cells.

Compared to the 3D-reconstruction technique, the stacking of Kelvin cells allows for the generation of different foam samples. However, as presented by Roberts & Garboczi [30], the anisotropic nature of the Kelvin cell results in the generation of a deterministic foam structure. Since real foams by nature exhibit the feature of randomness, it was initially deemed unable to describe such structures [30, 31]. This was partly remedied Habisreuther et al. [32]

by introducing randomness in the vertex positions of the multi-cell Kelvin model.

### 5.1.3 Voronoi tessellation and some generalizations

The last technique commonly used for foam generation is that of Voronoi tessellation. It is a space partitioning algorithm and is also sometimes referred to as the Voronoi diagram. The method revolves around a given set of points,  $\mathbf{p}$ , to generate (Voronoi) cell structures which adhere to [33]:

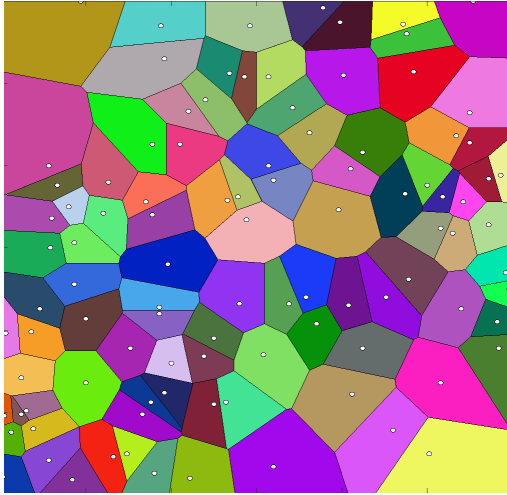
$$V(q, p_i) = \{\forall q \in R^n, d_V(q, p_i) < d_V(q, p_j), i \neq j\} \quad (1)$$

where  $d_V(q, p_i)$  is the Euclidean distance between points  $p_i$  and  $q$ :

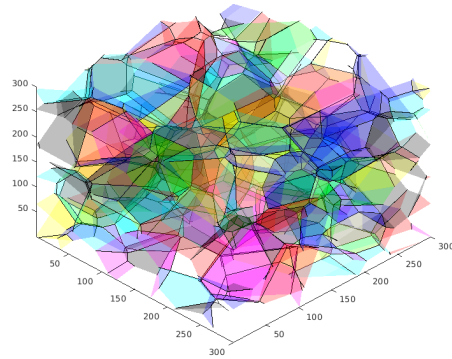
$$d_V(q, p_i) = \sqrt{(p_{i,x} - q_x)^2 + (p_{i,y} - q_y)^2 + (p_{i,z} - q_z)^2}$$

Voronoi diagrams based on other distance calculations, such as the Manhattan distance rather than the Euclidean distance, also exist.

The set of points,  $\mathbf{p}$ , are referred to as the generator, or seed, points with associated Voronoi cells,  $V(p_i)$ . These cells fulfill Eq. 1, which states that any point  $\mathbf{q}$  placed within the specific polygon  $i$  is closer to point  $\mathbf{p}_i$  than, any other generator point  $\mathbf{p}_j$ . The Voronoi diagrams with a random set of two and three dimensional points and associated cells are depicted in Fig 7.



(a) 2D Voronoi diagram.



(b) 3D Voronoi diagram.

Figure 7: Voronoi diagrams of random 2D and 3D seed points.

The Voronoi diagram algorithm presented within this section is specifically that of equal cell growth which only considers seed location. A more general



approach may also be used, e.g. the Laguerre-Voronoi tessellation, or power diagrams [34]. This type of tessellation instead takes a set of circle centers (spheres in three dimensions) as seed points, with the addition of using the circle radii as an extra term to calculate weighted distances.

## 5.2 Foam generation methods

Based on the three techniques presented, Voronoi-based methods were deemed as the most usable since they can be e.g. non-deterministic. They have also been previously used to great extent [5, 9–11] and were thus chosen as the foam generation method. However, additional algorithms are required to accurately determine the position of Voronoi cells. These algorithms should preferably take the following in account:

- Pore size and distribution from reconstructed tomographic data.
- Desired foam porosity or volume fraction.
- Sufficient packing density and distance between cell centers.

To fulfill these requirements, a method of Voronoi tessellation based on the force-biased sphere packing algorithm is used. This algorithm has been previously described [35, 36], with a somewhat modified version presented in the section below.

### 5.2.1 The (modified) force-biased sphere packing algorithm

The modified version initially uses an identical setup as the standard force-biased algorithm [35, 36]:

Start by placing  $N$  number of spheres within a cubic domain of length  $L$ . Sphere centre positions,  $\mathbf{r}_i$ , are initially positioned randomly, each with a diameter  $d_i$ , obtained from a chosen distribution.

The initial placement of spheres results in large overlaps between spheres which the force-biased algorithm aims to reduce. This algorithm is an iterative process which performs two major operations in each iteration, namely:

- Overlapping spheres are pushed apart with the help of a repulsive force.
- The diameter of all spheres is gradually shrunk with the help of a contraction equation.

To begin the process, normally all spheres are first assigned an outer and inner diameter,  $d_i^{out}$  and  $d_i^{in}$ , respectively. The outer diameter is initially

calculated from a volume-based equation while the inner diameter is taken as the smallest value of the distances between non-overlapping spheres.

For the modified version of this algorithm, only a single diameter,  $d^{sc}$ , is used to determine the interacting forces and change of contraction equation.

For all intents and purposes the scaling diameter,  $d^{sc}$ , is initially equal to the outer diameter used in the standard algorithm:

$$d^{sc} \equiv d^{out} = \left( \frac{6L^3 V_{nom}}{\pi \sum_{i=1}^N d_i^3} \right)^{1/3} \quad (2)$$

where  $V_{nom}$  is an volumetric input parameter determining the ratio between the sum of spherical volumes and the total volume of the cubic domain. To check for overlap a specific distance is used:

$$\|\mathbf{r}_i - \mathbf{r}_j\|_{current} < r_i + r_j$$

i.e., when the current distance between two points is less than the sum of corresponding sphere radii, overlap exists. The repulsive force between overlapping spheres is calculated from:

$$F_{ij} = \begin{cases} p_{ij} f_{\rho} \frac{\mathbf{r}_j - \mathbf{r}_i}{\|\mathbf{r}_j - \mathbf{r}_i\|}, & \text{if } \|\mathbf{r}_i - \mathbf{r}_j\|_{current} < r_i + r_j \\ 0, & \text{otherwise} \end{cases} \quad (3)$$

with a force scaling factor,  $f_{\rho}$ , and potential function,  $p_{ij}$ :

$$p_{ij} = d_i^{sc} d_j^{sc} \left( \frac{\|\mathbf{r}_i - \mathbf{r}_j\|^2}{\frac{1}{4}(d_i^{sc} + d_j^{sc})} - 1 \right)$$

The sum of total repulsive forces acting on a specific sphere is used to update the spherical center position according to:

$$\mathbf{r}_i := \mathbf{r}_i + \frac{1}{2d_i^{sc}} \sum_{j \neq i} F_{ij}$$

which also takes into account that larger spheres should move slower as compared to smaller spheres when affected by equal forces.

Lastly, the contraction equation is updated in each iterative step as:

$$d^{sc} := d^{sc} - \left( \frac{1}{2} \right)^{\delta} \frac{d_o^{sc}}{2\tau} \quad (4)$$

where  $\delta$  is the integer part of  $-\log_{10}(V_{\text{nom}} - V_{\text{act}})$ ,  $d_{st}^{out}$  is the start value of  $d_o^{sc}$  as per Eq. 2, and  $\tau$  is the scaling diameter contraction rate. Here the actual volume,  $V_{\text{act}}$ , is calculated as the ratio between the current sum of all spherical volumes and the volumetric domain. For the two dimensional case, the geometrical equivalent are disks.

The entire process of sphere pushing and diameter contraction is repeated until no overlap between spheres exists. After the algorithm converges, an additional step of removing spheres located outside of the original domain is performed. A 2D example based on a logarithmic-normal spherical diameter distribution are shown in Fig. 8a and 8b, before and after packing respectively.

### 5.2.2 The Voronoi tessellation of a sphere packing

Prior to determining the Voronoi tessellation of a provided sphere packing, an extra step is required to prevent the distortion and elongation of corresponding Voronoi cells. This is due to the cells at the boundaries of the original image otherwise stretching towards infinity. To remedy this effect, the system is made semi-infinite by repeating the all spheres periodically along the 26 possible combinations of x-,y-, and z-directions. In two dimensions, this instead corresponds to 8 repetitions along the x- and y-directions as depicted in Fig. 8c. As an example, the green colored disk originally positioned in the lower right corner of Fig. 8b has been mirrored in all directions. The final result is no longer a packing of spheres but solves the problem of distorted Voronoi cells.

The resulting periodic Voronoi diagram thus consists of 27 (9 in 2D) times the number of initial spheres obtained from the sphere packing algorithm. It can be visualized using the convex closure, or hull, of each corresponding Voronoi cell, shown in Fig. 8d. Additionally, for the three dimensional Voronoi Tessellation the Matlab routine *Mergecoplanarfaces* from *geom3d* [37] is used. The algorithm merges and re-orders any Voronoi vertices and positions which are co-planar within their respective cell.

### 5.2.3 Generating foam skeleton and image morphology

From Voronoi vertices and their connectivity, a skeleton of the foam material can be constructed. This is achieved by defining discretized vectors between all vertices within each convex hull. The vectors are mapped onto a 3D grid-based image, hereafter known as the foam skeleton, repeating the process for all Voronoi cells and associated vertices. This yields an image consisting of the Voronoi diagram copied onto an image. A two dimensional example is depicted in Fig. 8e.

Subsequently, morphological operations are performed on the obtained foam skeleton. These morphological operations correspond to the routines *imdilate* and *imclose* from the image processing toolbox in Matlab. These may also be referred to as filtering routines.

The *imdilate* routine takes an image and a structuring element as an input parameter, applying the element onto each voxel of an image. For the purpose of imitating tomography data, the structuring element chosen is a sphere of voxel radius  $r$ . This results in a system of cylindrical tubes, or struts, after the application of *imdilate*. Such a process may also be interpreted as a thickening of the provided image, as depicted in Fig. 8f.

To further mimic the properties of real foam materials, an additional image is created which considers the fact that foam vertices should be larger in size than foam struts. Therefore, dilation is performed solely on the vertex positions using a larger structuring element as compared to the foam skeleton. This "vertex" image is thereafter added to the already dilated foam skeleton yielding a combined image as seen in Fig. 8g.

Lastly, the *imclose* routine performs morphological closing of holes within an image. Similarly to the *imdilate* routine, it takes an image as well as a structuring element as input which are used to effectively close holes smaller (in voxel size) than the provided element. The closing process is applied to the combined dilated image of struts and vertices. This yields the final foam model depicted in Fig. 8h. An additional step of making a cylindrical cut of the final foam is performed to mimic the reconstructed foam shape, shown in Fig. 8i.

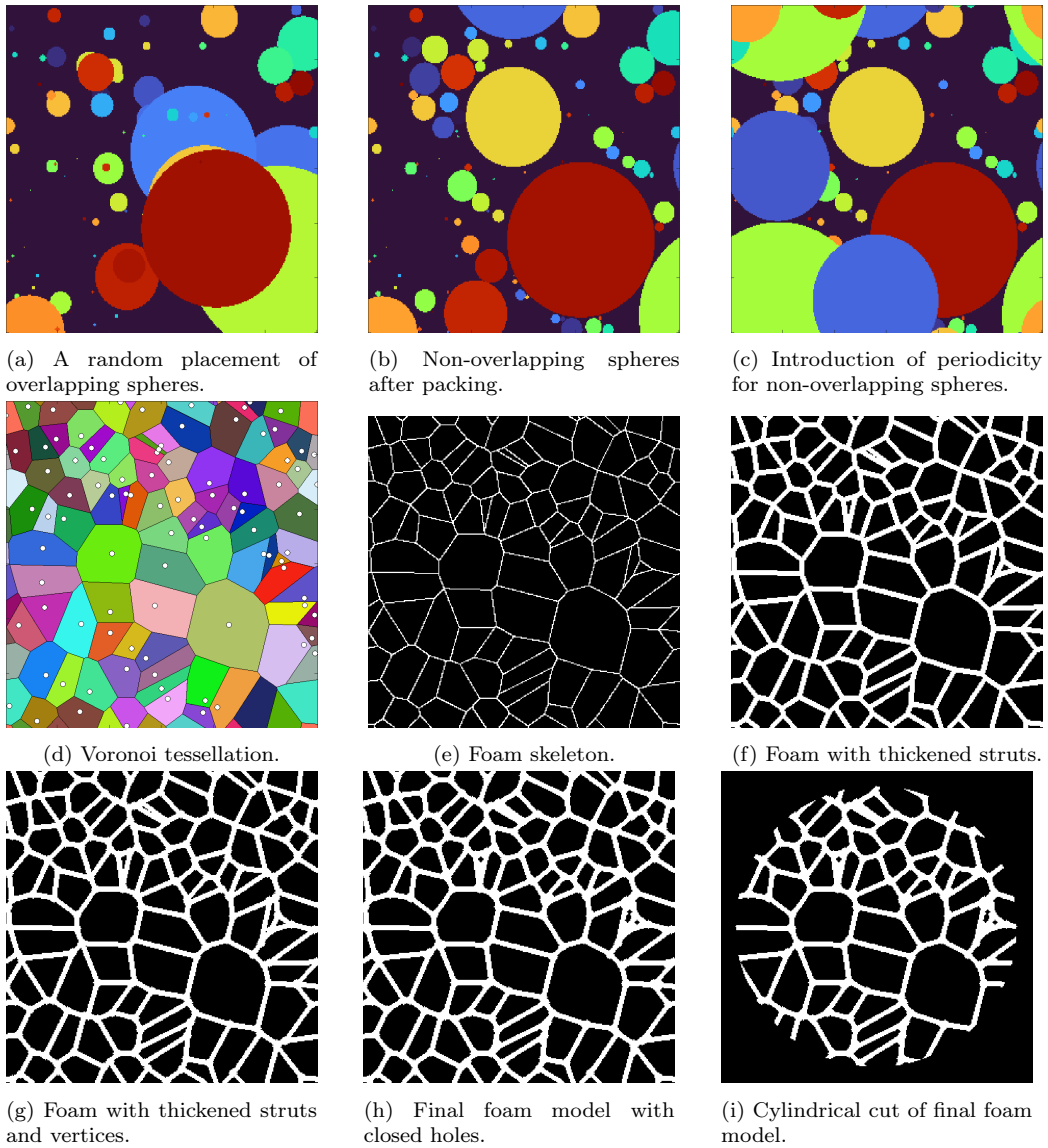


Figure 8: The full 2D Voronoi-based method based on a sphere packing. A random placement of spheres becomes non-overlapping, periodic and are used to create a Voronoi tessellation. The tessellation is converted to an image which is subject to image morphology. Lastly, a cylindrical cut of the model is made to mimic the reconstructed foam shape.

## 6 Mesh discretization

### 6.1 Meshing parameters and extraction

If the goal is to perform a FE-analysis on either the reconstructed or architecture foam model, appropriate finite element meshes are required. These can be generated using some mesh processing software. For the purpose of this thesis, iso2mesh [38] is chosen. It is an open source extension to Matlab which has the options to process, smoothen, clean, and create meshes from a provided image.

The meshing process is completed using the CGAL [39] option in iso2mesh which utilizes a weighted Delaunay triangulation to create either triangular (in 2D) or tetrahedral meshes (in 3D). CGAL takes the following input parameters: facet angle, facet size, facet distance, cell radius edge ratio, and cell size. In short, the three first parameters determine the minimum angle, size, and boundary approximation of surface mesh elements. The latter two are instead criteria regarding the shape and size of tetrahedral elements.

The obtained mesh can be exported from Matlab using the iso2mesh routine *saveabaqus*, which creates an .inp file containing mesh node positions and element connectivity. The resulting .inp file is imported into the finite element software Abaqus to perform thermal simulations.

### 6.2 Delaunay triangulation

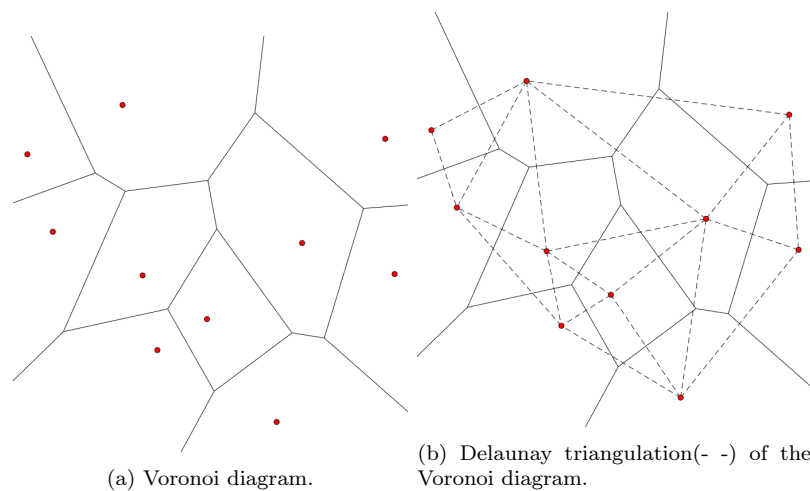


Figure 9: Voronoi, and Delaunay, triangulation of 10 randomly positioned seed points.

As previously mentioned, a method for creating tetrahedral meshes involves the use of Delaunay triangulation. It is a process in which a given number of points  $\mathbf{P}$  are connected via optimal triangulation [33]. The triangulation is closely related to the Voronoi diagram. The Delaunay triangulation is in fact the dual of the Voronoi diagram. In short, this means that the vertices of the Voronoi tessellation are the seed points of the Delaunay Triangulation and vice versa. The triangulation can therefore be constructed by connecting the points of all neighboring Voronoi cells. This creates triangular faces in two dimensions and tetrahedral cells in three dimensions, respectively. A Voronoi diagram and its associated Delaunay triangulation are shown in Fig. 9a and Fig. 9b, respectively.

## 7 Flowcharts of algorithms

Fig 10 shows the flowchart as a summary of the reconstruction and parameter extraction of tomography data samples. Similarly, Fig. 11 depicts the flowchart process used for the generation of architectural foam models.

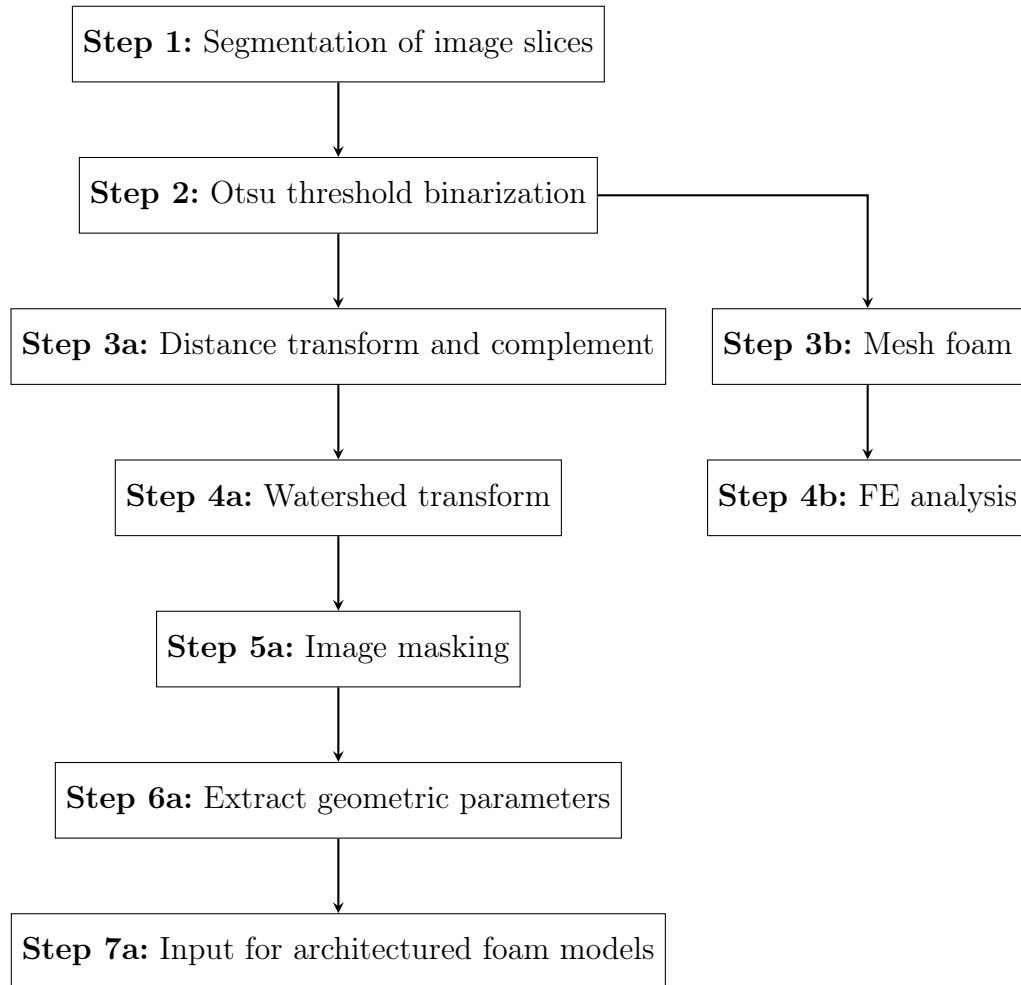


Figure 10: Flowchart of tomography data - reconstruction and parameter extraction.



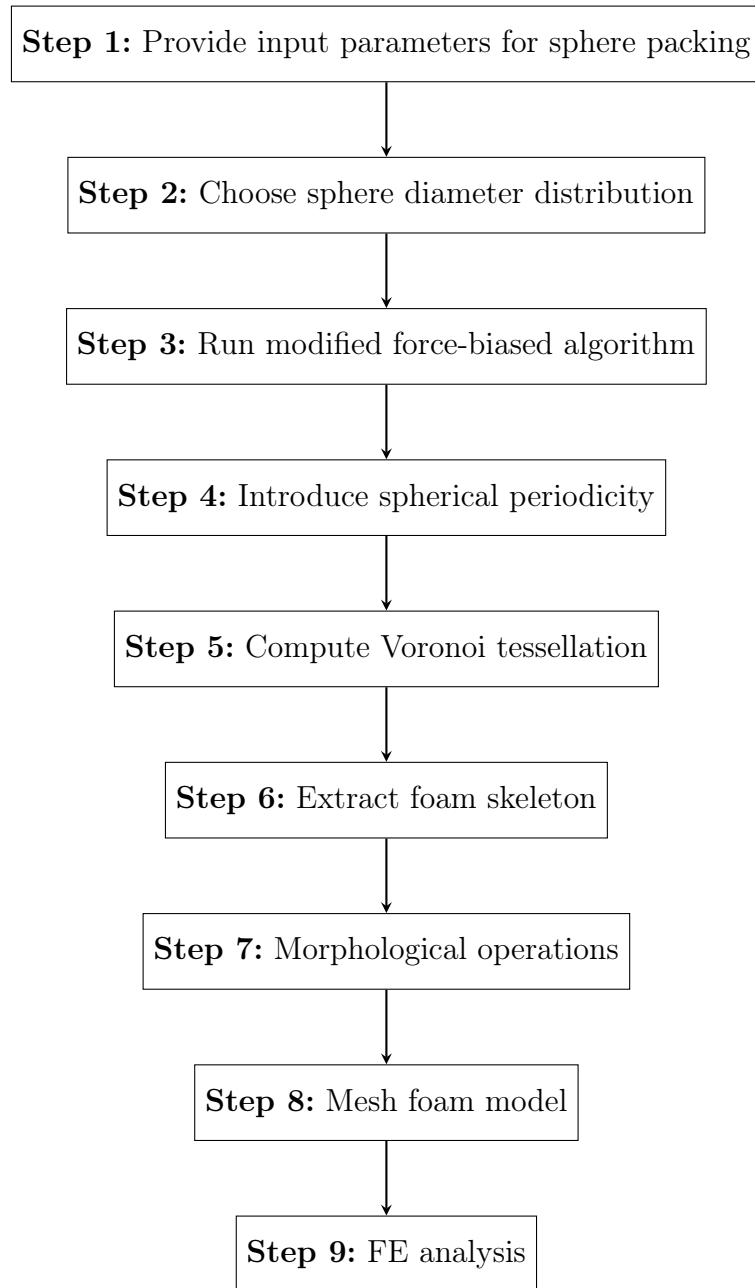


Figure 11: Flowchart of architectural foam generation model.

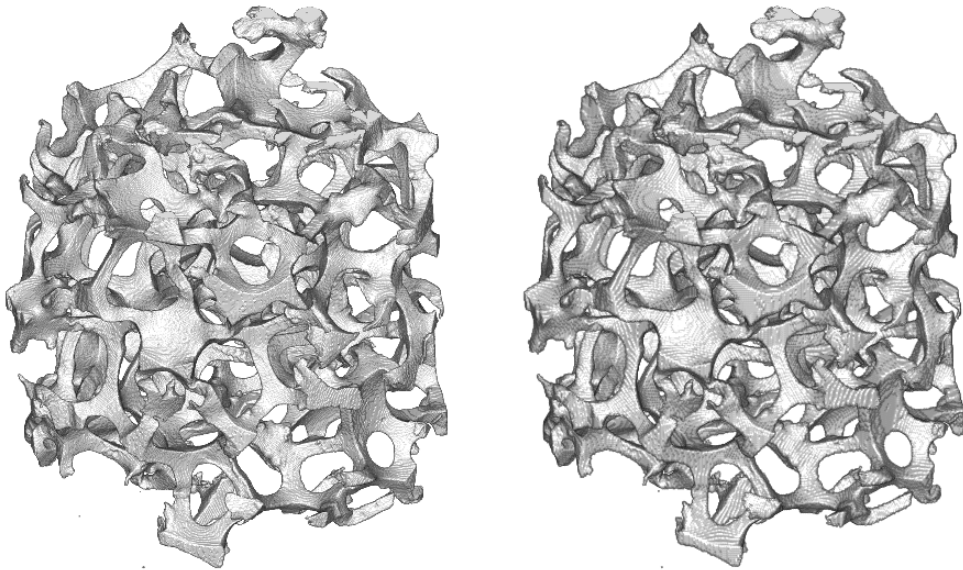
## 8 Results and discussion

### 8.1 Reconstructed tomography data

Using the method outlined in Section 4.1, a three dimensional reconstruction of the tomographic foam data is assembled. The size of the tomography data is  $1232 \times 1340 \times 1079$  voxels. Additionally, each voxel in the sample is  $6 \mu\text{m}$ . This corresponds to a volume of size  $0.74 \times 0.65 \times 0.8 \text{ cm}^3$ .

Furthermore, to reduce computational time required, the image size is reduced by half and a quarter, respectively. This is also due to the utilized computer lacking sufficient virtual memory to perform operations on the full  $1232 \times 1340 \times 1079$  image.

The resulting images are of size  $616 \times 670 \times 540$  and  $308 \times 335 \times 270$ . The corresponding reconstructions are shown in Fig 12a and Fig 12b. These reconstructions will also be referred to as the larger( $616 \times 670 \times 540$ ) and smaller( $308 \times 335 \times 270$ ) image further on.



(a) Reconstruction of size  $616 \times 670 \times 540$ .

(b) Reconstruction of size  $308 \times 335 \times 270$ .

Figure 12: 3D-reconstruction of tomography data using different image sizes.

Table 1: Parameters obtained from image processing of tomography data.

Image size	Intensity cut-off	Porosity	Pores	Pore radius
1232×1340×1079	17780	91.7 %	-	-
616×670×540	17642	91.7 %	65	71.6941
308×335×270	17758	91.74 %	46	42.2611

Table 1 presents parameters for different image sizes. Intensity cut-off and porosity are found with the Otsu binarization and porosity method presented in Section 4.1. Meanwhile, the number of pores and pore radii are extracted using the distance-watershed transform described in Sections 4.2.1 and 4.2.2. Again, since the foam investigated is of cylindrical shape, the sum of data points is taken as a cylinder rather than a box. That is, image voxels outside this cylinder are not considered for the porosity calculations. An identical approach is taken when extracting the number of pores and pore radius.

The extracted pore radii for all samples are in the units of voxels. It was not possible to extract the pore and pore radius for the full image due to a lack of virtual memory.

Based solely on the obtained intensity cut-off and porosity, it would be probably be sufficient to use extracted values from the image of size 308×335×270. The difference is about 0.5 % while the intensity threshold is actually closer to full image as compared to the larger image. However, when comparing the pore number and pore radii, it becomes clear that further differences exist between reconstructed samples.

By considering that the larger image is twice the size of the smaller image in each of the x-, y-, and z-directions, the extracted radius should be twice as large for the 616×670×540 image. That is, a pore of radius  $R$  in Fig. 12b would have a radius of  $2R$  in Fig. 12a. This does not seem to be the case with the radius ratio instead being  $71.6841/42.2611 \approx 1.5$ . A similar ratio is obtained for the number of pores.

One possible explanation might be that since only a quarter of the initial data is considered for the smaller image, separate pores become connected when performing the distance-watershed transform. For the larger image they would instead have been distinguished as separate pores.

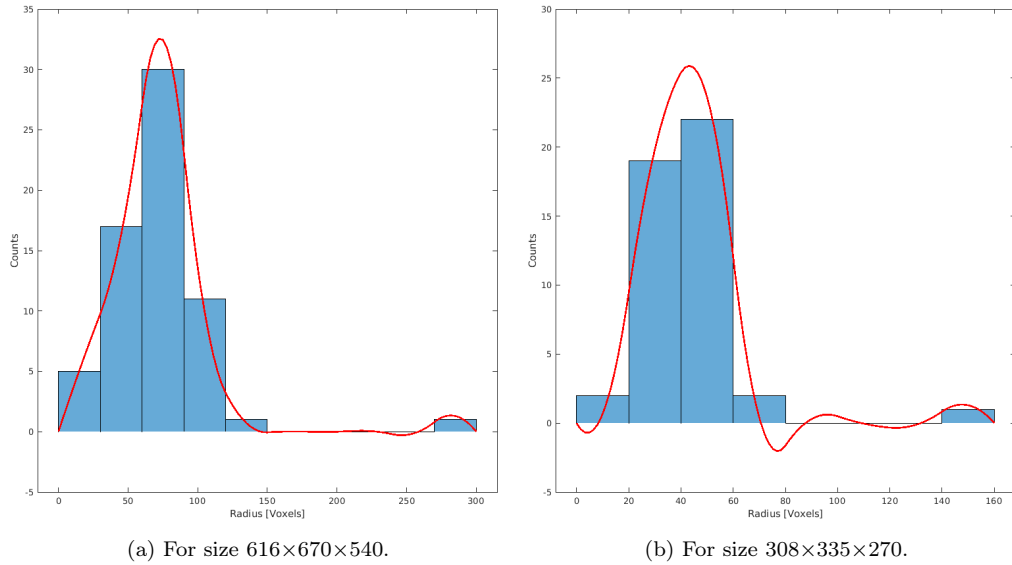


Figure 13: Pore radial distribution histograms of reconstructed foam samples.

The pore radius obtained from the distance-watershed transform is actually a radial distribution. The average of this distribution is presented in Table 1. Corresponding pore radial distributions are plotted and shown in Fig. 13 for both the larger and smaller reconstructed foam sample.

By visually examining the plots, it would seem that the distribution is either of a Gaussian or similar shape. This is similar to previous research [5, 8] which specifically used either a Gaussian or log-normal distribution as the spherical diameter distribution. The small intensity peak located far away on the x-axis likely corresponds to the volume outside the cylindrical foam and should therefore not be considered.

## 8.2 Architected foam samples

Architected foams based on a Voronoi tessellation in combination with a force-biased sphere packing of size 300x300x300 are generated. The obtained foam skeleton is subjected to image morphology, resulting in a final foam model.

Different samples are created by varying the input parameters of the sphere packing algorithm. These parameters are the spherical diameter distribution, number of spheres, sphere radii, volumetric input parameter, force scaling factor, and contraction rate presented in Section 5.2.1.

The spherical diameter distributions are chosen based on diameter distributions obtained from the reconstructed foams and previous research. Taking into account the reconstructed data distributions, the log-normal and Gaussian distributions are therefore mainly investigated.

For each distribution, the effect of varying the number of spheres and resulting spherical radii is studied. The impact of the remaining parameters,  $V_{nom}$ ,  $f_p$ , and  $\tau$  on the resulting foam is also considered for a single distribution. Corresponding porosity, number of pores, and pore radii are extracted with the same algorithms used for the tomographic data, i.e. with binarization and distance-watershed transforms.

Unless otherwise state the default values used for the sphere packing algorithm are:  $f_p = 0.3$ ,  $\tau = 4 \times 10^6$ , and  $V_{nom} = 1$ . For all distributions, five different number of spheres are considered: 40, 80, 120, 160, and 200.

### 8.2.1 Log-normal distribution

For the log-normal distribution, the mean and variance are chosen as one and two, respectively. This is in agreement with values outlined in the original force-biased algorithm [35, 36]. The resulting foam porosity and average pore radius as a function of the number of spheres are shown in Table 2.

Table 2: Parameters of architected log-normal distribution.

Spheres	Porosity	Average pore radii	Pores
40	93.79 %	48.1563	35
80	90.95 %	44.0088	53
120	88.17 %	39.9206	76
160	86.69 %	38.8299	71
200	84.91 %	37.2607	74

Based on the values obtained from the log-normal distributions, it is evident that a larger number of spheres results in a lower foam porosity, i.e. a higher

relative density. Since each sphere added to the algorithm corresponds to the addition of an extra Voronoi cell to the final foam model, this should come as no surprise.

On the other hand, the average pore radius decreases as the number of spheres increase. Considering that the volume of the domain remains constant, the volume of each pore must decrease to accommodate an increasing number of them. If the volume of each pore decreases, so does its radius since they are directly correlated.

The architected log-normal foam sample are depicted in Fig. 14 - 16, with an increasing number of spheres. The corresponding figure to each such sample is also provided in Table 2. In addition, the reconstructed foam sample is shown in Fig. 16b for visual comparison.

From examining the results, it seems a larger number of spheres are required to achieve similar porosity as the reconstructed foam. A similar observation is made regarding the pore radius. This could be partly due to the randomness in the model, partly due to the previously mentioned problems regarding the watershed transform.

Additionally, from both a visual and numerical comparison such as porosity, it seems the optimal number of spheres is around 80 to achieve similar results in terms of e.g. porosity. In order to match both porosity and pore radius, additional rigorous testing of distribution values is required.

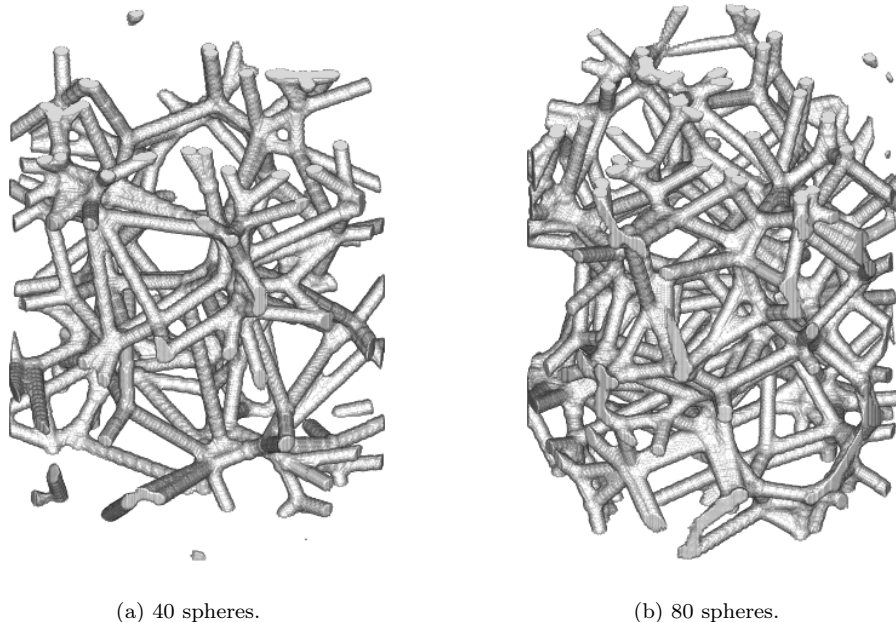
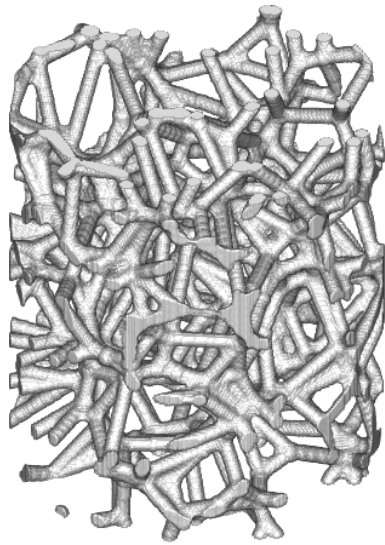
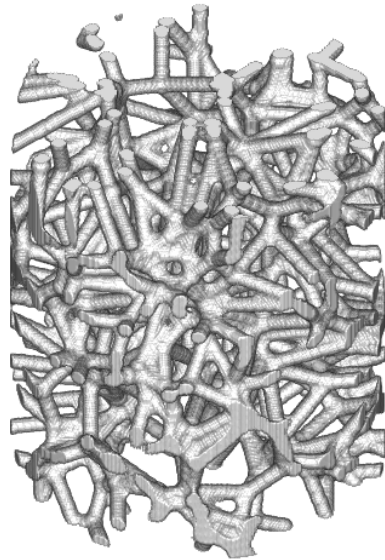


Figure 14: Architected foams based using a log-normal spherical diameter distribution with number of spheres equal to 40 and 80, respectively.

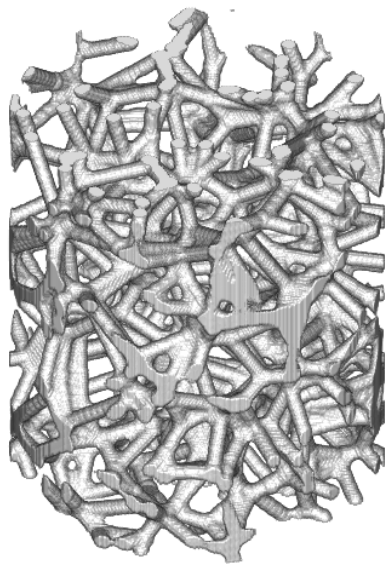


(a) 120 spheres.

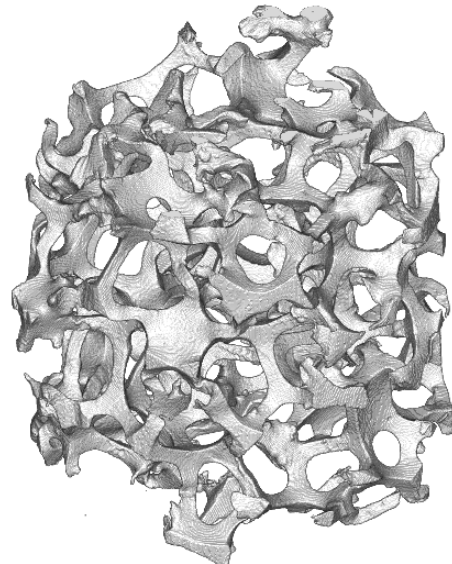


(b) 160 spheres.

Figure 15: Architected foams based using a log-normal spherical diameter distribution with number of spheres equal to 120 and 160, respectively.



(a) 200 spheres.



(b) Reconstructed foam.

Figure 16: Architected foam based using a log-normal spherical diameter distribution with number of spheres equal to 200. Shown is also the reconstructed foam, 16b.

The impact of changing the remaining parameters is also investigated, i.e.  $V_{nom}$ ,  $f_p$ , and  $\tau$ . That is the, volumetric input parameter, force scaling factor, and contraction rate of the sphere packing algorithm presented in Section 5.2.1. Table 3 presents the changes in porosity and pore radius obtained by varying the volumetric parameter, force scale factor, and contraction rate. The values in the top row of the table is obtained by using default parameters.

Table 3: The impact of sphere packing parameters, volumetric input, force scaling factor, and contraction rate.

Spheres	$V_{nom}$	$f_p$	$\tau$	Porosity	Pore radius
80	1.0	0.3	$4 \times 10^6$	90.95 %	44.0088
80	<b>0.2</b>	0.3	$4 \times 10^6$	90.39 %	45.7342
80	<b>0.4</b>	0.3	$4 \times 10^6$	90.71 %	43.9160
80	<b>0.6</b>	0.3	$4 \times 10^6$	91.52 %	48.0462
80	<b>0.8</b>	0.3	$4 \times 10^6$	90.66 %	43.0423
80	1.0	<b>0.2</b>	$4 \times 10^6$	90.83 %	43.4997
80	1.0	<b>0.4</b>	$4 \times 10^6$	90.79 %	44.4649
80	1.0	<b>0.6</b>	$4 \times 10^6$	90.90 %	43.4015
80	1.0	<b>0.8</b>	$4 \times 10^6$	90.51 %	45.5218
80	1.0	<b>1.0</b>	$4 \times 10^6$	91.21 %	42.8701
80	1.0	0.3	$4 \times 10^3$	90.71 %	45.0904
80	1.0	0.3	$4 \times 10^4$	90.93 %	45.6304
80	1.0	0.3	$4 \times 10^5$	91.56 %	47.0716
80	1.0	0.3	$4 \times 10^7$	90.56 %	44.1762

By comparison, it seems these parameters only affect the porosity and pore radius slightly, if at all. The largest differences between values obtained from using default parameters are approximately 9 % for the pore radius and 7 % for the porosity. They are due to a change in volumetric parameter, from 1 to 0.6, and contraction rate, from  $4 \times 10^6$  to  $4 \times 10^5$ , respectively. Additionally, no direct correlation can be seen between changes in porosity and radius by either increasing or decreasing parameter values. As an example, changing the value of  $V_{nom}$  from 0.2 to 0.4 decreases the pore radius. However, increasing it one additional step suddenly increases the radius. A similar response is observed for the other parameters. The small differences might be accredited to the fact that the spheres are initially positioned randomly in the packing algorithm. As such, no two simulations will be identical when providing the same input parameters. Together with the fact that the differences are small to begin with, it was deemed unnecessary to evaluate these three parameters for additional distributions.



### 8.2.2 Gaussian distribution

The Gaussian, or normal, distribution is also considered. Mean and variance values are five and two, respectively. Extracted parameters are presented in Table 4. In addition, similar to the log-normal distribution, foams generated from a different number of spheres are shown in Fig. 17-19. The reconstructed sample is once again used for visual comparison, depicted in Fig 19b.

Table 4: Extracted parameters of Gaussian distribution foam.

Spheres	Porosity	Average pore radius	Pores
40	94.62 %	53.2501	36
80	91.69 %	45.3129	57
120	89.93 %	42.4004	63
160	87.16 %	38.7808	80
200	85.55 %	35.5741	91

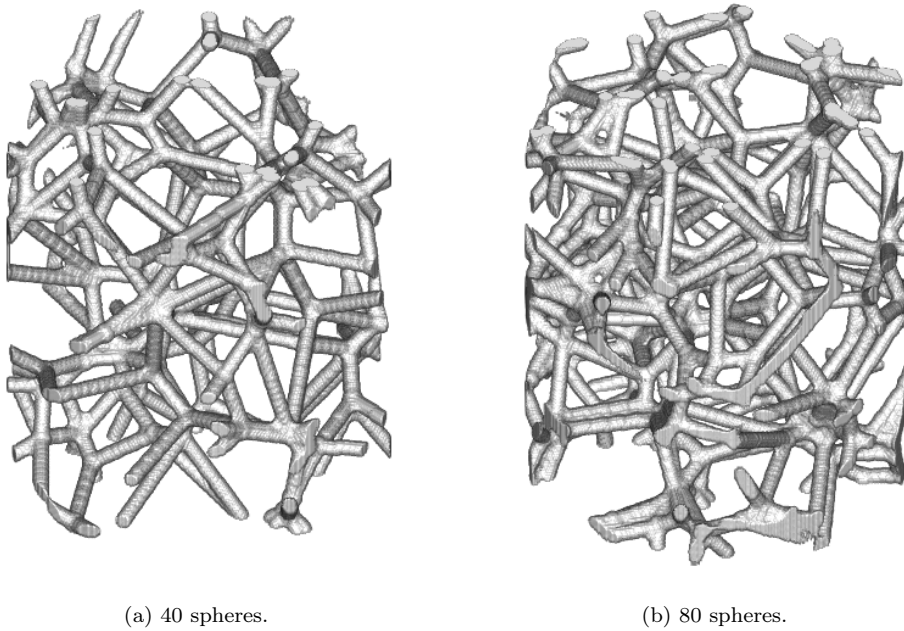
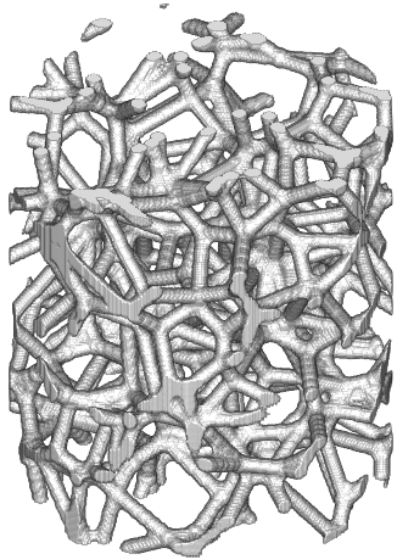
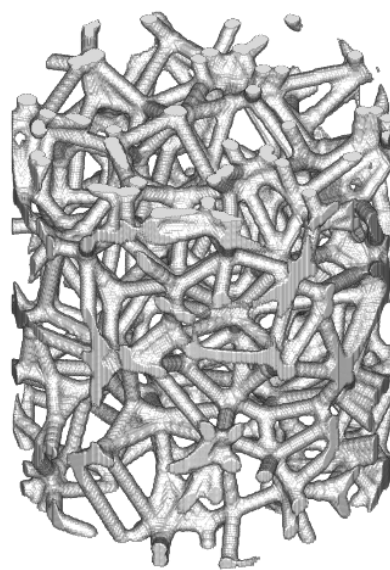


Figure 17: Architected foams based using a Gaussian spherical diameter distribution with number of spheres equal to 40 and 80, respectively.

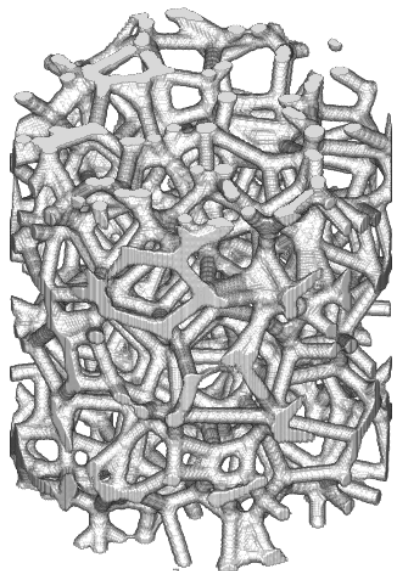


(a) 120 spheres.

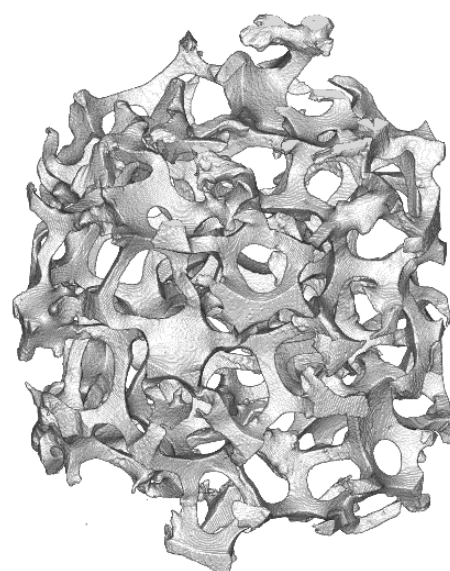


(b) 160 spheres.

Figure 18: Architected foams based using a Gaussian spherical diameter distribution with number of spheres equal to 40 and 80, respectively.



(a) 200 spheres.



(b) Reconstructed foam.

Figure 19: Architected foam based using a Gaussian spherical diameter distribution with number of spheres equal to 200. Shown is also the reconstructed foam, 19b.

A similar trend as for the log-normal distribution is observed. That is, an increase in the number of spheres results in lower porosity, i.e. a higher relative density, but a decrease of pore radius. The reason may be partly the same as for the other distribution. However, while the trend remains the same, the values do not. Specifically, both the porosity and pore radii are on average lower for an equal number of spheres. This could be partly due to the mean and variance values chosen and partly due to the properties of each distribution.

### 8.2.3 Additional distributions

In addition to the log-normal and Gaussian distributions, two additional diameter distributions are considered. These are the two-point (with diameter ratio of 1:10) and uniform (with values between 1 and 10) distributions. For every distribution the porosity and corresponding pore size are plotted and shown in Fig. 20a and Fig. 20b, respectively.

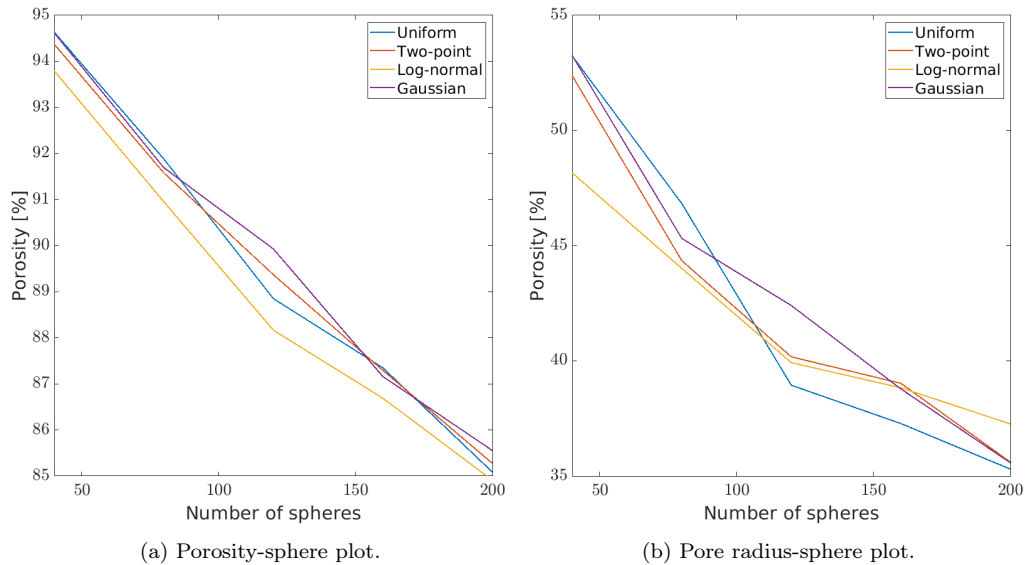


Figure 20: Porosity and pore radius as a function of the number of spheres.

From both plots, an approximately linear relation between parameters can be seen. Additionally, the differences between each distribution are quite small for both the porosity and pore radii. These could be explained by the fact that there always exists randomness in the structure due to the random initial positions of spheres. This means that performing the simulations again with identical parameters will yield different results. These new values may very well be close, or even equal to, the values obtained from any other

distributions. Therefore, it may be actually enough to consider only a single distribution with either the log-normal or Gaussian distribution being the most likely candidate. This is partly due to these distributions previously being used in Voronoi tessellations of random sphere packings [5, 9, 18].

### 8.3 Finite element mesh generation

A few different combinations of mesh parameters are considered as inputs for the meshing software iso2mesh. The main goal is to reduce the number of elements while trying to maintain a good description of the original model. By varying each parameter twice, a total of 11 different meshes are obtained. The top row of values corresponds to a mesh created using the default values in iso2mesh. No value exists for the cell size in the algorithm but a value of 10 is chosen. The number of elements presented is of tetrahedral. Table 5 and Table 6 display data obtained by using the larger and smaller reconstructed foam models, respectively.

Table 5: Table of mesh parameters for the large reconstructed image. Angle is in degrees while sizes are in units of pixels for facets and voxels for cells.

Angle	Facet size	Distance	Edge ratio	Cell size	Elements
30	6	0.5	3	10	978 892
<b>10</b>	6	0.5	3	10	543 913
<b>20</b>	6	0.5	3	10	574 808
30	<b>2</b>	0.5	3	10	1 417 796
30	<b>10</b>	0.5	3	10	992 161
30	6	<b>1.0</b>	3	10	222 349
30	6	<b>1.5</b>	3	10	143 174
30	6	0.5	<b>6</b>	10	938 060
30	6	0.5	<b>9</b>	10	939 327
30	6	0.5	3	<b>50</b>	976 422
30	6	0.5	3	<b>100</b>	976 487

Table 6: Table of mesh parameters for the small reconstructed image. Angle is in degrees while sizes are in units of pixels for facets and voxels for cells.

Angle	Facet size	Distance	Edge ratio	Cell size	Elements
30	6	0.5	3	10	242 235
<b>10</b>	6	0.5	3	10	150 865
<b>20</b>	6	0.5	3	10	157 709
30	<b>2</b>	0.5	3	10	315 391
30	<b>10</b>	0.5	3	10	245 532
30	6	<b>1.0</b>	3	10	71 672
30	6	<b>1.5</b>	3	10	37 785
30	6	0.5	<b>6</b>	10	241 910
30	6	0.5	<b>9</b>	10	241 899
30	6	0.5	3	<b>50</b>	242 135
30	6	0.5	3	<b>100</b>	242 111

The tetrahedral mesh of the larger reconstructed image created using default parameters is shown in Fig. 21a. Fig. 21b instead depicts the coarsest mesh obtained from Table 5. That is, using the following values: facet angle = 30, facet size = 6, facet distance = 1.5, cell edge ratio = 3, and cell size = 10.

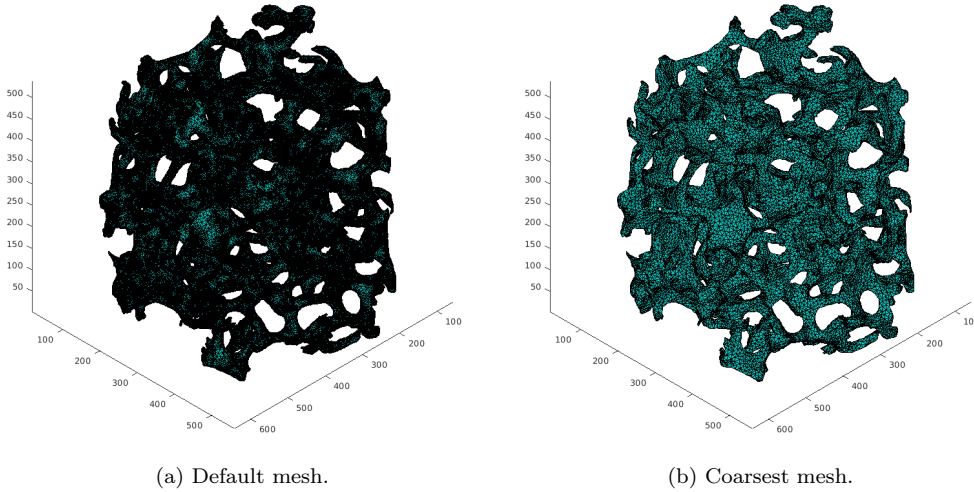


Figure 21: Default and coarse mesh for the  $616 \times 640 \times 540$  reconstructed foam of Table 5.

Mesh data for the two architected foams based on log-normal and Gaussian distributions are presented in Table 7 and Table 8, respectively. Corresponding meshes can be found in the Appendix.

Table 7: Table of mesh parameters for the log-normal distribution foam. Angle is in degrees while sizes are in units of pixels for facets and voxels for cells.

Angle	Facet size	Distance	Edge ratio	Cell size	Elements
30	6	0.5	3	10	215 042
<b>10</b>	6	0.5	3	10	153 761
<b>20</b>	6	0.5	3	10	153 165
30	<b>2</b>	0.5	3	10	294 137
30	<b>10</b>	0.5	3	10	214 454
30	6	<b>1.0</b>	3	10	59 309
30	6	<b>1.5</b>	3	10	33 027
30	6	0.5	<b>6</b>	10	221 150
30	6	0.5	<b>9</b>	10	221 153
30	6	0.5	3	<b>50</b>	215 033
30	6	0.5	3	<b>100</b>	214 976

Table 8: Table of mesh parameters for the Gaussian distribution foam. Angle is in degrees while sizes are in units of pixels for facets and voxels for cells.

Angle	Facet size	Distance	Edge ratio	Cell size	Elements
30	6	0.5	3	10	208 721
<b>10</b>	6	0.5	3	10	146 289
<b>20</b>	6	0.5	3	10	148 712
30	<b>2</b>	0.5	3	10	283 103
30	<b>10</b>	0.5	3	10	207 302
30	6	<b>1.0</b>	3	10	57 673
30	6	<b>1.5</b>	3	10	31 947
30	6	0.5	<b>6</b>	10	214 976
30	6	0.5	<b>9</b>	10	215 039
30	6	0.5	3	<b>50</b>	208 751
30	6	0.5	3	<b>100</b>	208 709

The role of each mesh parameter has been briefly described in Section 6, with additional information available in the CGAL Documentation [39]. The effect of changing each parameter will be shortly discussed as well as their impact on the number of elements and geometrical properties.

By changing the facet angle, to 10 instead of the default 30, a dramatic decrease in element number is achieved. A similar response is seen for a value of 20, with both values resulting in about a 40-45 % decrease.

Even though decreasing the facet angle reduces the number of elements, it may also have other consequences. The reason is that this value determines

the minimum angle of a surface element. Therefore, a lower angle would result in surface elements becoming more elongated and more prone to distortion.

For the facet size, the resulting mesh numbers are quite intuitive. By decreasing the size of each surface element, more elements are required to properly mesh the foam. The opposite response is achieved by increasing the facet size, at least to a certain degree. Depending on the size of the geometry used, increasing the facet size will not result in less elements.

Varying the facet distance has an extremely large impact on the number of mesh elements, even more so than changing the facet angle. By simply increasing it from the default value of 0.5 to 1.5, the number of mesh elements is reduced by approximately 77 %. However, the price to be paid is that the constructed mesh surface is a poor description of the original foam surface.

This could mean that, e.g. small nooks and crannies which may be of importance to the microstructural response, will not be considered. Even parts of larger structures will be ignored by increasing the facet distance even further.

As for the cell edge ratio, a slight change in the number of elements is obtained by increasing this value. Similar to the facet angle, this parameter determines the shape of elements, but for 3D rather than 2D. Also, a similar effect is achieved by increasing this value as for the facet angle: the creation of elongated tetrahedral elements.

Lastly, the cell size plays a very similar role as the facet size. That is, as the cell size decreases, additional volume elements are required to mesh the same model. Thus, the number of elements increases. The opposite is achieved by increasing the cell size.

Similar relations between mesh parameters and the resulting number of mesh elements can be found for all models used.

From the simulations performed, the largest difference in the number of mesh elements was obtained by varying the facet distance. Similar decreases in number of elements are obtained for all models. Based on all simulations the quickest way to reduce the number of mesh elements is to increase the facet distance with the price of possibly removing important parts of the structure. By trial and error, it would probably be possible to find a value with a good balance between element reduction and surface approximation.

The other alternative is to reduce the facet angle but create poorly defined elements.

## 8.4 Thermal analysis

For the purpose of showing that it is possible to successfully go from the reconstructed or architected foam to a final FE simulation, a thermal

analysis of a few samples are performed. Simulation setup is fairly simple: The top of sample is assigned a constant temperature of  $T = 500K$  while the bottom is kept at room temperature ( $T = 300K$ ). Furthermore, the problem is solved assuming non-transient, i.e. steady-state, conditions. Simulations are performed using the coarsest mesh for each image in Tables 6 - 8.

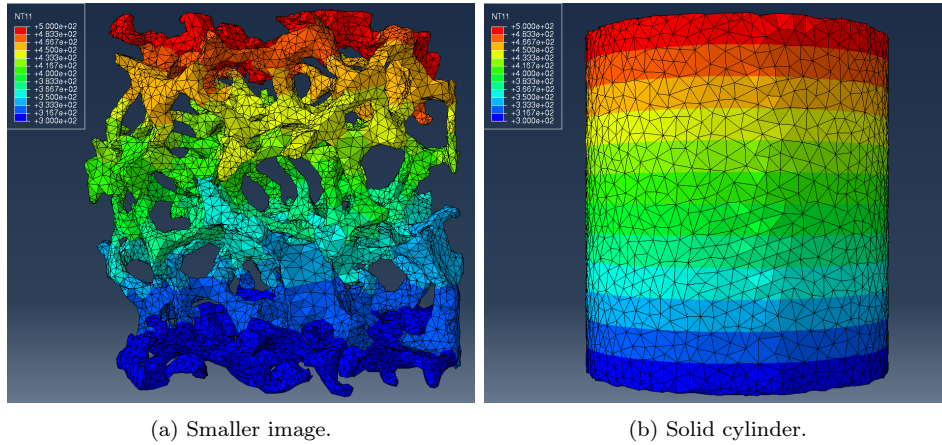


Figure 22: Temperature distribution of the smaller image and a solid cylinder.

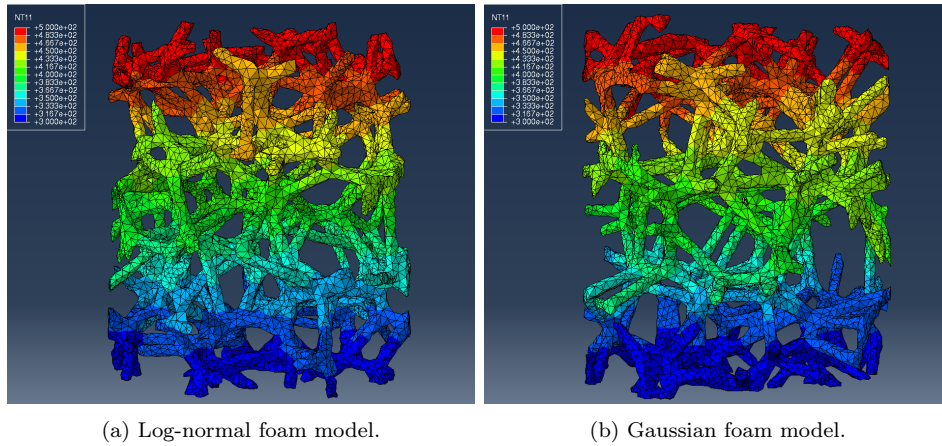


Figure 23: Temperature distribution of log-normal and Gaussian foam models.

The temperature distribution for a reconstructed foam sample and a solid cylinder are shown in Fig. 22a and Fig. 22b, respectively. Additionally, Fig. 23a and Fig. 23b depict the same distribution for the log-normal and Gauss architected models.



## 9 Conclusions and future work

As the concluding remarks of this thesis project, the reconstruction and foam generation models have been successful. The chosen generation method of Voronoi tessellation produces foam models with similar porosity and pore radius as the reconstructed foam model. However, more work is required on the subsequent image morphology. A simple process of thickening struts and vertices of the foam skeleton was used. Another approach would have been a distance-based morphology function to mimic nature. This routine would add larger spheres closer to the foam vertices. In contrast, thinner spheres would be added along the struts, with a gradual increase in between struts and vertices. Other possibilities would be changing the structuring element to another geometrical object based on the shape of reconstructed foam struts.

For additional complexity, a different Voronoi tessellation based method, such as those based on weighted expansion, might have been considered.

Lastly, by showing that it is possible to reconstruct CT samples, mesh, and perform FE-simulations on the models, additional paths can be explored within this field. An example would be mechanical simulations in regards to metal foam microstructural behaviour.

## References

- [1] Letícia Filice, Francesco Gagliardi, and Domenico Umbrello. “Simulation of aluminum foam behavior in compression tests”. In: *Arabian Journal for Science and Engineering* 34 (June 2009).
- [2] A. Carofalo, Marta Giorgi, and Anna Morabito. “Geometric modelling of metallic foams”. In: *Engineering Computations: Int J for Computer-Aided Engineering* 30 (Oct. 2013). DOI: [10.1108/EC-06-2011-0070](https://doi.org/10.1108/EC-06-2011-0070).
- [3] Yasin Amani et al. “Thermal conductivity of highly porous metal foams: Experimental and image based finite element analysis”. In: *International Journal of Heat and Mass Transfer* 122 (2018), pp. 1–10. ISSN: 0017-9310. DOI: <https://doi.org/10.1016/j.ijheatmasstransfer.2018.01.050>.
- [4] Quinton C. Johnson et al. “Mapping 3D grain and precipitate structure during in situ mechanical testing of open-cell metal foam using micro-computed tomography and high-energy X-ray diffraction microscopy”. In: *Materials Characterization* 195 (2023), p. 112477. ISSN: 1044-5803. DOI: <https://doi.org/10.1016/j.matchar.2022.112477>.
- [5] Lukas Bogunia, Stefan Buchen, and Kerstin Weinberg. “Microstructure characterization and stochastic modeling of open-cell foam based on  $\mu$ CT-image analysis”. In: *GAMM-Mitteilungen* 45.3-4 (2022), e202200018. DOI: <https://doi.org/10.1002/gamm.202200018>.
- [6] Christophe Leblanc et al. “Analysis of an open foam generated from computerized tomography scans of physical foam samples”. In: *International Journal for Numerical Methods in Engineering* 123.18 (2022), pp. 4267–4295. DOI: <https://doi.org/10.1002/nme.7008>.
- [7] A. Liebscher et al. “Stochastic Multiscale Modeling of Metal Foams”. In: *Procedia IUTAM* 6 (2013). IUTAM Symposium on Multiscale Problems in Stochastic Mechanics, pp. 87–96. ISSN: 2210-9838. DOI: <https://doi.org/10.1016/j.piutam.2013.01.010>.
- [8] C. Lautensack et al. “Modelling a ceramic foam using locally adaptable morphology”. In: *Journal of Microscopy* 230.3 (2008), pp. 396–404. DOI: <https://doi.org/10.1111/j.1365-2818.2008.01998.x>.
- [9] Zhengwei Nie, Yuyi Lin, and Qingbin Tong. “Modeling structures of open cell foams”. In: *Computational Materials Science* 131 (2017), pp. 160–169. ISSN: 0927-0256. DOI: <https://doi.org/10.1016/j.commatsci.2017.01.029>.

- [10] Zhigang Fan et al. “Simulation of polycrystalline structure with Voronoi diagram in Laguerre geometry based on random closed packing of spheres”. In: *Computational Materials Science* 29.3 (2004), pp. 301–308. ISSN: 0927-0256. DOI: <https://doi.org/10.1016/j.commatsci.2003.10.006>.
- [11] T. Wejrzanowski et al. “Structure of foams modeled by Laguerre–Voronoi tessellations”. In: *Computational Materials Science* 67 (2013), pp. 216–221. ISSN: 0927-0256. DOI: <https://doi.org/10.1016/j.commatsci.2012.08.046>.
- [12] C Motz and Reinhard Pippan. “Deformation behaviour of closed-cell aluminium foams in tension”. In: *Acta Materialia* 49 (Aug. 2001), pp. 2463–2470. DOI: [10.1016/S1359-6454\(01\)00152-5](https://doi.org/10.1016/S1359-6454(01)00152-5).
- [13] Thomas Kalpakoglou and Stylianos Yiatros. “Metal foams: A review for mechanical properties under tensile and shear stress”. In: *Frontiers in Materials* 9 (Oct. 2022), p. 998673. DOI: [10.3389/fmats.2022.998673](https://doi.org/10.3389/fmats.2022.998673).
- [14] L.J. Gibson and M.F. Ashby. *Cellular solids: Structure and properties, second edition*. (1)Department of Materials Science and Engineering, Massachusetts Institute of Technology: Cambridge University Press, 2014. ISBN: 9781139878326.
- [15] “Chapter 2 - Making metal foams”. In: *Metal Foams*. Ed. by M.F. Ashby et al. Burlington: Butterworth-Heinemann, 2000, pp. 6–23. ISBN: 978-0-7506-7219-1. DOI: <https://doi.org/10.1016/B978-075067219-1/50004-0>.
- [16] Ramvir Singh and H.S Kasana. “Computational aspects of effective thermal conductivity of highly porous metal foams”. In: *Applied Thermal Engineering* 24.13 (2004), pp. 1841–1849. ISSN: 1359-4311. DOI: <https://doi.org/10.1016/j.applthermaleng.2003.12.011>.
- [17] Paola Ranut. “On the effective thermal conductivity of aluminum metal foams: Review and improvement of the available empirical and analytical models”. In: *Applied Thermal Engineering* 101 (2016), pp. 496–524. ISSN: 1359-4311. DOI: <https://doi.org/10.1016/j.applthermaleng.2015.09.094>.
- [18] Claudia Lautensack et al. “3D characterization, modeling, and effective thermal conductivity of open aluminum foams, 3D-Charakterisierung”. In: *Their Physical and Mechanical Properties, ICAA, International Conference on Aluminium Alloys, 11* (2008), pp. 1368–1374.

- [19] P.S. Liu and G.F. Chen. “Chapter Nine - Characterization Methods: Basic Factors”. In: *Porous Materials*. Ed. by P.S. Liu and G.F. Chen. Boston: Butterworth-Heinemann, 2014, pp. 411–492. ISBN: 978-0-12-407788-1. DOI: <https://doi.org/10.1016/B978-0-12-407788-1.00009-5>.
- [20] P.S. Liu and G.F. Chen. “Chapter Two - Making Porous Metals”. In: *Porous Materials*. Ed. by P.S. Liu and G.F. Chen. Boston: Butterworth-Heinemann, 2014, pp. 21–112. ISBN: 978-0-12-407788-1. DOI: <https://doi.org/10.1016/B978-0-12-407788-1.00002-2>.
- [21] Bisma Parveez et al. “Microstructure and Mechanical Properties of Metal Foams Fabricated via Melt Foaming and Powder Metallurgy Technique: A Review.” In: *Materials* 15.15 (2022). ISSN: 1996-1944. DOI: 10.3390/ma15155302.
- [22] G.J. Davies and S. Zhen. “Metallic foams: their production, properties and applications.” In: *Journal of Materials Science* 18 (1983), pp. 1899–1911. DOI: <https://doi.org/10.1007/BF00554981>.
- [23] P.S. Liu and G.F. Chen. “Chapter Three - Application of Porous Metals”. In: *Porous Materials*. Boston: Butterworth-Heinemann, 2014, pp. 113–188. ISBN: 978-0-12-407788-1. DOI: <https://doi.org/10.1016/B978-0-12-407788-1.00003-4>.
- [24] Luc Salvo et al. “3D imaging in material science: Application of X-ray tomography”. In: *Comptes Rendus Physique* 11.9 (2010). Interactions between radiofrequency signals and living organisms, pp. 641–649. ISSN: 1631-0705. DOI: <https://doi.org/10.1016/j.crhy.2010.12.003>.
- [25] Cristian T. Badea. “Chapter 4 - Principles of Micro X-ray Computed Tomography”. In: *Molecular Imaging (Second Edition)*. Ed. by Brian D. Ross and Sanjiv Sam Gambhir. Second Edition. Academic Press, 2021, pp. 47–64. ISBN: 978-0-12-816386-3. DOI: <https://doi.org/10.1016/B978-0-12-816386-3.00006-5>.
- [26] Carmignato S. et al. Withers P.J. Bouman C. “X-ray computed tomography”. In: *Nat Rev Methods Primers* 1.18 (2021). DOI: <https://doi.org/10.1038/s43586-021-00015-4>.
- [27] Makoto Iizuka et al. “Large Deformation Finite Element Analyses for 3D X-ray CT Scanned Microscopic Structures of Polyurethane Foams”. In: *Materials* 14.4 (2021). ISSN: 1996-1944. DOI: 10.3390/ma14040949.
- [28] Nobuyuki Otsu. “A Threshold Selection Method from Gray-Level Histograms”. In: *IEEE Transactions on Systems, Man, and Cybernetics* 9.1 (1979), pp. 62–66. DOI: 10.1109/TSMC.1979.4310076.

- [29] William Thomson. “On the division of space with minimum partitioned area”. In: *Acta Mathematica* 11.none (1887), pp. 121–134. DOI: 10.1007/BF02612322. URL: <https://doi.org/10.1007/BF02612322>.
- [30] A.P. Roberts and E.J. Garboczi. “Elastic moduli of model random three-dimensional closed-cell cellular solids”. In: *Acta Materialia* 49.2 (2001), pp. 189–197. ISSN: 1359-6454. DOI: [https://doi.org/10.1016/S1359-6454\(00\)00314-1](https://doi.org/10.1016/S1359-6454(00)00314-1).
- [31] H.X. Zhu, N.J. Mills, and J.F. Knott. “Analysis of the high strain compression of open-cell foams”. In: *Journal of the Mechanics and Physics of Solids* 45.11 (1997), pp. 1875–1904. ISSN: 0022-5096. DOI: [https://doi.org/10.1016/S0022-5096\(97\)00027-6](https://doi.org/10.1016/S0022-5096(97)00027-6).
- [32] P. Habisreuther, N. Djordjevic, and N. Zarzalis. “Statistical distribution of residence time and tortuosity of flow through open-cell foams”. In: *Chemical Engineering Science* 64.23 (2009), pp. 4943–4954. ISSN: 0009-2509. DOI: <https://doi.org/10.1016/j.ces.2009.07.033>.
- [33] Franz Aurenhammer, Rolf Klein, and Der-Tsai Lee. *Voronoi Diagrams and Delaunay Triangulations*. 2013. DOI: 10.1142/8685.
- [34] F Aurenhammer. “Power Diagrams: Properties, Algorithms and Applications”. In: *SIAM Journal on Computing* 16.1 (Feb. 1987), pp. 78–96. ISSN: 0097-5397. DOI: 10.1137/0216006.
- [35] Monika Bargieł and Jacek Mościński. “C-language program for the irregular close packing of hard spheres”. In: *Computer Physics Communications* 64.1 (1991), pp. 183–192. ISSN: 0010-4655. DOI: [https://doi.org/10.1016/0010-4655\(91\)90060-X](https://doi.org/10.1016/0010-4655(91)90060-X).
- [36] Alexander Bezrukov, Monika Bargieł, and Dietrich Stoyan. “Statistical Analysis of Simulated Random Packings of Spheres”. In: *Particle & Particle Systems Characterization* 19.2 (2002), pp. 111–118. DOI: [https://doi.org/10.1002/1521-4117\(200205\)19:2<111::AID-PPSC111>3.0.CO;2-M](https://doi.org/10.1002/1521-4117(200205)19:2<111::AID-PPSC111>3.0.CO;2-M).
- [37] David Leglend (2023). *geom3d*, *MATLAB Central File Exchange*. visited on 2023-05-24. URL: <https://www.mathworks.com/matlabcentral/fileexchange/24484-geom3d>.
- [38] Anh Phong Tran, Shijie Yan, and Qianqian Fang. “Improving model-based functional near-infrared spectroscopy analysis using mesh-based anatomical and light-transport models”. In: *Neurophotonics* 7 (Feb. 2020), p. 1. DOI: 10.1117/1.NPh.7.1.015008.

- [39] Pierre Alliez et al. “3D Mesh Generation”. In: *CGAL User and Reference Manual*. 5.5.2. CGAL Editorial Board, 2023. URL: <https://doc.cgal.org/5.5.2/Manual/packages.html#PkgMesh3>.

# Appendix

## Additional meshes

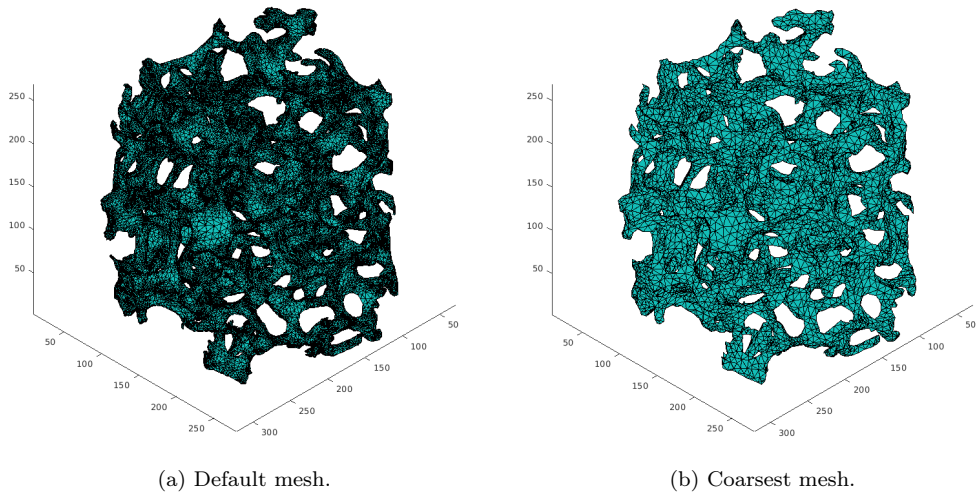


Figure 24: Meshes of smaller reconstructed image using default parameters and parameters producing the coarsest mesh from Table 6.

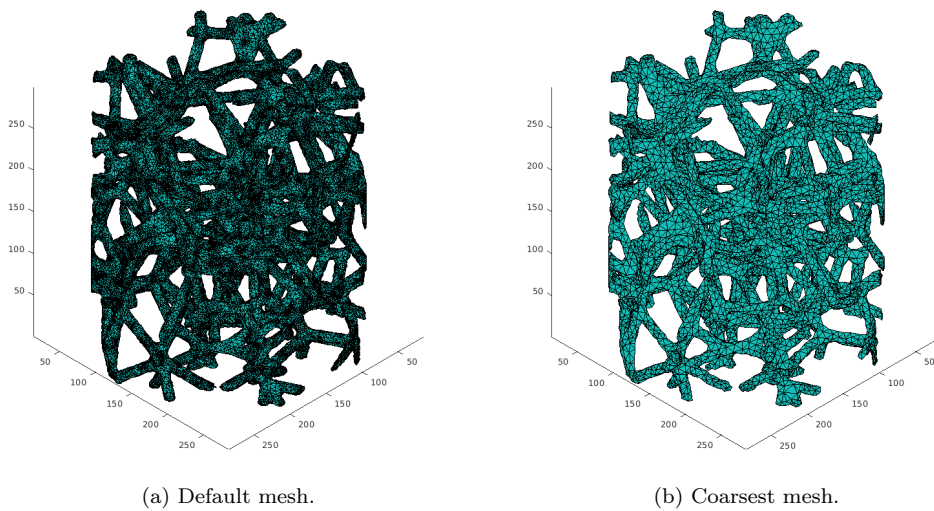
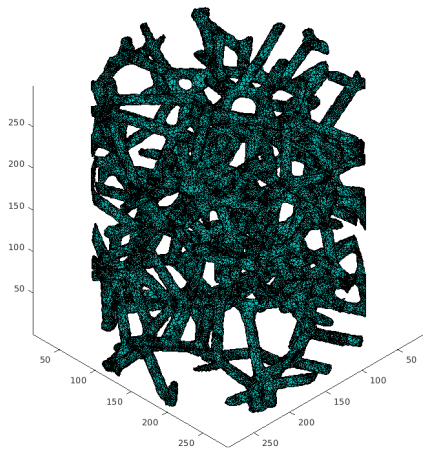
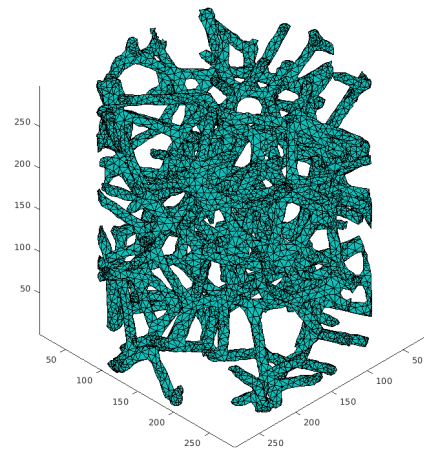


Figure 25: Meshes of architected log-normal model using default parameters and parameters producing the coarsest mesh from Table 7.



(a) Default mesh.



(b) Coarsest mesh.

Figure 26: Meshes of architected Gaussian model using default parameters and parameters producing the coarsest mesh from Table 8.